Meghan Lentz

Candidate

Physics and Astronomy

Department

This dissertation is approved, and it is acceptable in quality and form for publication:

Approved by the Dissertation Committee:

David Dunlap , Chairperson

Joshua Townsend

Susan Atlas

Keith Lidke

A Systematic Approach to the Characterization of Liquid-Vapor Coexistence in Platinum

by

Meghan Kathleen Lentz

B.S., Physics, Syracuse University, 2017
B.S., Applied Mathematics, Syracuse University, 2017

THESIS

Submitted in Partial Fulfillment of the
Requirements for the Degree of

Doctor of Philosophy
Physics

The University of New Mexico

Albuquerque, New Mexico

July, 2025

Acknowledgements

Thank you to my various colleagues at Sandia National Laboratories for all of the guidance and encouragement throughout this process. This dissertation would not have been possible without the help I have received from Amanda Dumi, Cody Melton, Kyle Cochrane, Ray Clay, and Martha Mitchell. Thank you most of all to my advisor, Josh Townsend, I cannot express in words how grateful I am for your mentorship, patience, and kindness. I know I am a much better scientist today thanks to the time and care you have expended to me. I would also like to thank my family, particularly my parents for the unending support and love they have given me throughout my entire life. Lastly, thank you so much to my dear brother, William Lentz II, for being a Wall street sellout, allowing me to be the first in our family to receive a doctorate degree.

Disclaimer: Sandia National Laboratories is a multi-mission laboratory managed and operated by National Technology & Engineering Solutions of Sandia, LLC, a wholly owned subsidiary of Honeywell International Inc., for the U.S. Department of Energy's National Nuclear Security Administration under contract DE-NA0003525. This paper describes objective technical results and analysis. Any subjective views or opinions that might be expressed in the paper do not necessarily represent the views of the U.S. Department of Energy or the United States Government.

A Systematic Approach to the Characterization of Liquid-Vapor Coexistence in Platinum

by

Meghan Kathleen Lentz

B.S., Physics, Syracuse University, 2017
B.S., Applied Mathematics, Syracuse University, 2017

PhD, Physics, University of New Mexico, 2025

Abstract

Platinum is an unreactive transition metal that does not experience any experimentally observed solid-solid phase transitions from its face-centered cubic (fcc) crystal structure below melt. Platinum is a material standard frequently used for high pressure and shock compression experiments at Sandia National Laboratories. During these experiments, materials are subjected to a very large range of thermodynamic conditions, during which materials can regularly enter the liquid-vapor coexistence region. Despite its status as a material standard, the region around the liquid-vapor critical point is poorly understood for platinum, with reported critical temperatures spanning approximately 7000 K. In order to accurately predict experiments that encounter these phases, knowing the location of the liquid-vapor phase boundary is paramount. For general material design, understanding liquid-vapor coexistence and phase transitions is vital when considering the efficiency and safety of products utilizing these materials. Additionally, many industrial chemical processes rely on the vaporization and distillation of materials.

In this dissertation we conduct density functional theory based molecular dynamics (DFTMD) simulations for platinum for a range of temperatures and densities near liquid-vapor coexistence. The phase diagram for platinum is refined near the critical point using two independent techniques for analyzing the DFTMD data. The first technique includes fitting the DFTMD results to an equation of state (EOS) in order to calculate the critical point. The phase boundary is then characterized by performing a Maxwell construction. The second technique utilizes an instantaneous interface calculation to divide the volume into two distinct phases. We find that the two approaches result in a critical point and liquid-vapor phase boundary that agree well. We also find that our analyses agree within error with recent experimental measurements of the liquid side of the phase boundary of platinum. With the improved characterization of the coexistence region, we then investigate the electrical conductivity of platinum in this region of phase space using the Kubo-Greenwood approximation. We find that the calculated effective DC conductivity is heavily influenced by the geometry of the system.

Contents

List of Figures

List of Tables

Chapter 1

Introduction

Material characterization is a fundamental research endeavor that influences almost every aspect of modern life. It is through the understanding of material properties that there exists continued innovation of new and old technologies. The advances in material development and design are so ubiquitous in society and the manufacturing processes so streamlined that they are often treated as expendable. But it has been the culmination of decades of concentrated research efforts dedicated to understanding and adequately representing the complex quantum mechanical processes underlying material behaviors. Material characterization can be approached both experimentally, through laboratory measurements, and theoretically, through materials modeling. From the materials modeling field there are a wide range of techniques using mathematical models to describe materials in order to predict properties quantitatively. The focus of this work will be on computational materials modeling from first principles, starting from fundamental theoretical axioms, using density functional theory (DFT) molecular dynamics to predict material properties based on the electronic configuration. Much of this work emphasizes the existence of an interdis-

ciplinary crossroad, wherein the application of fundamental concepts of materials science, physics and chemistry are only realizable through the use of high performance computing architectures employing applied mathematics and numerical analysis procedures.

1.1 Electronic Structure Theory

To understand how a material's bulk properties relate to its electronic configuration, it is necessary to have a solid understanding of electronic structure theory. Electronic structure theory focuses on the quantum mechanical treatment of atoms and electrons that determine physical and chemical properties of matter. The motion and position of a single electron is described by the Schrödinger equation [12]; for the purposes of this work, we will only be considering the time-independent Schrödinger equation [13]:

$$\Big[-\sum_{i=1}^{N}\frac{\hbar^2}{2m_e}\nabla_i^2+V(\mathbf{r})\Big]\Psi(\mathbf{r})=E\Psi(\mathbf{r}). \tag{1.1}$$

Here, $\hbar$ is the reduced Planck constant and m_e is the electron mass. The sum over i is the sum over all N electrons. The first term inside the bracketed expression represents the kinetic energy of the electrons, while $V(\mathbf{r})$ is the potential energy and $\mathbf{r}$ represents all particles in the system.

Considering a molecular system, the Schrödinger equation must describe the interactions and positions of many interacting electrons and nuclei. Replacing the first term of equation 1.1, the kinetic energy for a system of N electrons and M nuclei is

$$-\sum_{i=1}^{N}\frac{\hbar^2}{2m_e}\nabla_i^2-\sum_{j=1}^{M}\frac{\hbar^2}{2M_j}\nabla_j^2, \tag{1.2}$$

where m_j is the mass of the j^{th} nucleus.

To define the potential energy in the many-body Schrödinger equation, the interactions between the different types of particles need to be accounted for. The Coulomb repulsion between electrons for $\hat{N}$ is represented by [14]:

$$\frac{e^2}{8\pi\epsilon_0}\sum_{i\neq i'}^{N}\frac{1}{|\mathbf{r}_i-\mathbf{r}_{i'}|}, \tag{1.3}$$

where e is the electron charge and ε_0 is the permittivity of vacuum. Similarly, the Coulomb repulsion between nuclei is:

$$\frac{e^2}{8\pi\epsilon_0}\sum_{j\neq j'}^{M}\frac{Z_jZ_{j'}}{|\mathbf{R}_j-\mathbf{R}_{j'}|}, \tag{1.4}$$

where Z_j is the atomic number of the j^{th} nucleus. Finally, the Coulomb attraction between electrons and nuclei is:

$$-\frac{e^2}{4\pi\epsilon_0}\sum_{i}^{N}\sum_{j}^{M}\frac{Z_j}{|\mathbf{r}_i-\mathbf{R}_j|}. \tag{1.5}$$

From Equations 1.2, 1.3, 1.4, 1.5 the many-body Schrödinger equation is written as [15]:

$$\Bigg[-\sum_{i=1}^{N}\frac{\hbar^2}{2m_e}\nabla_i^2-\sum_{j=1}^{M}\frac{\hbar^2}{2M_j}\nabla_j^2+\frac{1}{2}\sum_{i\neq i'}^{N}\frac{e^2}{4\pi\epsilon_0}\frac{1}{|\mathbf{r}_i-\mathbf{r}_{i'}|}$$

$$+\frac{1}{2}\sum_{j\neq j'}^{M}\frac{e^2}{4\pi\epsilon_0}\frac{Z_jZ_{j'}}{|\mathbf{R}_j-\mathbf{R}_{j'}|}-\sum_{i}^{N}\sum_{j}^{M}\frac{e^2}{4\pi\epsilon_0}\frac{Z_j}{|\mathbf{r}_i-\mathbf{R}_j|}\Bigg]\Psi=E_{tot}\Psi, \tag{1.6}$$

where Ψ is a function of the position vectors of the electrons and ions, $\Psi(\mathbf{r};\mathbf{R})$, and E_{tot} is the total energy of the system.

Solving the many-body Schrödinger equation scales exponentially. Because the wave-function for N particles depends on the complete N-dimensional configuration space, the number of variables needed to describe the quantum system scales as 3^N. Conversely, we need only $6N$ variables to describe a classical system. This results in a problem that is impossible to solve with current computational tools for all but the simplest of systems. In order to represent the system in a way that is solvable quantifiably, some approximations need to be made.

1.1.1 Hartree Atomic Units

Before continuing on with our discussion, we first take a moment to consider the units of measurement being used. The expression in equation 1.6 contains several fundamental physical constants that are independent of the material under consideration, namely:

- the reduced Planck constant, $\hbar = 1.0545718 \cdot 10^{-34}$ J $\cdot$ s
- the electron mass, $m_e = 9.1093837 \cdot 10^{-31}$ kg
- the proton mass, $m_p = 1.6726219 \cdot 10^{-27}$ kg
- the electron charge, $e = 1.6021766 \cdot 10^{-19}$ C

- the permittivity of vacuum, $\epsilon_0 = 8.8541878 \cdot 10^{-12}$ F/m

For convenience, we consider the average electron orbital radius for the hydrogen atom, $a_0 \simeq 0.5291772$ Å, where one angstrom, Å, is 10^{-10} m. With this, along with equations 1.3-1.5, we find an estimate for the Coulomb energy between particle pairs, also referred to as the Hartree energy:

$$E_{Ha} \simeq \frac{e^2}{4\pi\epsilon_0 a_0} = 27.211386 \text{ eV}, \tag{1.7}$$

where "Ha" stands for Hartree. A typical magnitude of the potential energy terms in equation 1.6 is of order E_{Ha}. Similarily, we find that the kinetic energy terms are also of the order E_{Ha}. Considering the angular momentum and force balancing for the hydrogen atom [16], we find

$$m_e v a_0 = \hbar \tag{1.8}$$

and

$$m_e \frac{v^2}{a_0} = \frac{e^2}{4\pi\epsilon_0 a_0} \tag{1.9}$$

$$\implies \frac{1}{2} m_e v^2 = \frac{1}{2} E_{Ha}. \tag{1.10}$$

Because all of the terms in equation 1.6 are of the order E_{Ha}, we can divide the entire expression by this quantity, giving us a simplified expression that describes energies in

units E_{Ha}, distances in units a_0, and masses in units of m_e, also referred to as atomic units. Within this Hartree unit scheme, the value of the electron charge, e, and mass, m_e are 1. In Hartree atomic units, the many-body Schrödinger equation takes the form [15]:

$$\left[-\sum_{i=1}^{N} \frac{\nabla_i^2}{2} - \sum_{i=1}^{M} \frac{\nabla_j^2}{2M_j} - \sum_{i}^{N} \sum_{j}^{M} \frac{Z_j}{|\mathbf{r}_i - \mathbf{R}_j|} + \frac{1}{2} \sum_{i \neq i'}^{N} \frac{1}{|\mathbf{r}_i - \mathbf{r}_{i'}|} + \frac{1}{2} \sum_{j \neq j'}^{M} \frac{Z_j Z_{j'}}{|\mathbf{R}_j - \mathbf{R}_{j'}|} \right] \Psi = E_{tot} \Psi, \tag{1.11}$$

1.1.2 Born-Oppenheimer Approximation

A common technique for simplifying equation 1.11 is to implement the Born-Oppenheimer approximation [17]. Because the nuclei are much more massive than the electrons, they move more slowly than the electrons. Therefore, the coordinates of the nuclei can be approximated as being fixed in place with respect to the electrons. In other words, the wavefunction representing the system can be separated into two independent wavefunctions, one representing the electron coordinates and one the coordinates of the nuclei:

$$\Psi_{total} = \psi_{electronic} \Phi_{nuclear} \tag{1.12}$$

Within this approximation, the nuclear kinetic energy can be calculated separately such that the ion dynamics are determined by the ground-state electronic wavefunction. This allows us to neglect the ion-ion term in the Hamiltonian. Applying this to equation 1.11, the many-body Schrödinger equation is simplified to:

$$\left[-\sum_{i=1}^{N} \frac{\nabla_i^2}{2} - \sum_{i}^{N} \sum_{j}^{M} \frac{Z_j}{|\mathbf{r}_i - \mathbf{R}_j|} + \frac{1}{2} \sum_{i \neq i'}^{N} \frac{1}{|\mathbf{r}_i - \mathbf{r}_{i'}|} \right] \psi = E \psi, \tag{1.13}$$

where $\psi = \psi_{electronic.}$ This new energy, E, is defined as the total energy from equation 1.11 with the ion-ion contribution removed:

$$E = E_{tot} - \frac{1}{2}\sum_{j\neq j'}^{M}\frac{Z_j Z_{j'}}{|\mathbf{R}_j - \mathbf{R}_{j'}|}. \tag{1.14}$$

1.1.3 Independent Electrons Approximation

Even with the simplifications from the Born-Oppenheimer approximation, equation 1.13 is still too complex to solve outside of the simplest systems. To simplify this expression further, additional approximations must be made. Within equation 1.13, the only term representing interactions between electrons is the Coulomb repulsion term, therefore removing this term would result in a system where the electrons do not interact. This simplification is called the independent electron equation [15]. Because the electrons are independent the probability of finding electron 1 at $\mathbf{r}_1$, *and* electron 2 at $\mathbf{r}_2$, ... *and* electron N at $\mathbf{r}_N$ becomes the product of the individual probabilities of finding the i^{th} electron at position $\mathbf{r}_i$:

$$|\psi(\mathbf{r}_1, \mathbf{r}_2, ..., \mathbf{r}_N)|^2 = |\phi_1(\mathbf{r}_1)|^2 |\phi_2(\mathbf{r}_2)|^2 ... |\phi_N(\mathbf{r}_N)|^2, \tag{1.15}$$

where $|\phi_i(\mathbf{r}_i)|^2$ is the probability of finding electron i at $\mathbf{r}_i$.

Assuming that the now independent electron wavefunctions are the solutions to the single-particle Schrödinger equation:

$$\sum_{i}^{N}\hat{H}_{0,i}(\mathbf{r}_i)\phi_i(\mathbf{r}_i) = \varepsilon_i\phi_i(\mathbf{r}_i), \quad \hat{H}_{0,i}(\mathbf{r}_i) = -\frac{1}{2}\nabla_i^2 - \sum_{j}^{M}\frac{Z_j}{|\mathbf{r}_i - \mathbf{R}_j|} \tag{1.16}$$

where $\hat{H}_0$ is the single electron Hamiltonian. Considering again the Schrödinger equation that represents the entire system, plugging in equation 1.15:

$$\Big[\sum_i \hat{H_{0,i}}(\mathbf{r}_i)\Big]\phi_1(\mathbf{r}_1)\phi_2(\mathbf{r}_2)...\phi_N(\mathbf{r}_N) = E\phi_1(\mathbf{r}_1)\phi_2(\mathbf{r}_2)...\phi_N(\mathbf{r}_N), \tag{1.17}$$

which can be further separated

$$\big[\hat{H_{0,1}}(\mathbf{r}_1)\phi_1(\mathbf{r}_1)\big]\phi_2(\mathbf{r}_2)...\phi_N(\mathbf{r}_N) + \phi_1(\mathbf{r}_1)\big[\hat{H_{0,2}}(\mathbf{r}_2)\phi_2(\mathbf{r}_2)\big]...\phi_N(\mathbf{r}_N) + ... = E\phi_1(\mathbf{r}_1)...\phi_N(\mathbf{r}_N) \tag{1.18}$$

From equation 1.16, we find:

$$E = \varepsilon_1 + \varepsilon_2 + ... + \varepsilon_N. \tag{1.19}$$

While we have significantly simplified the problem with the addition of the independent electron approximation, there are important issues that need to be addressed within this approximation.

1.1.4 Fermion Wavefunctions

The Pauli exclusion principle states that two or more fermions cannot simultaneously occupy the same quantum state [13]. Within the independent electron approximation discussed in the previous section, equation 1.15 does not obey the Pauli exclusion principle. For example, given a system of two electrons, the wavefunction $\psi(\mathbf{r}_1, \mathbf{r}_2) = \phi_1(\mathbf{r}_1)\phi_2(\mathbf{r}_2)$,

where $\mathbf{r}_1 \neq \mathbf{r}_2$ does not satisfy $\psi(\mathbf{r}_1,\mathbf{r}_2) \neq \psi(\mathbf{r}_2,\mathbf{r}_1)$, nor the proper spin statistics. However, the normalized wavefunction form:

$$\psi(\mathbf{r}_1,\mathbf{r}_2) = \frac{1}{\sqrt{2}}\big[\phi_1(\mathbf{r}_1)\phi_2(\mathbf{r}_2) - \phi_1(\mathbf{r}_2)\phi_2(\mathbf{r}_1)\big], \tag{1.20}$$

satisfies the spin statistics condition, such that $\psi(\mathbf{r}_1,\mathbf{r}_2) = -\psi(\mathbf{r}_2,\mathbf{r}_1)$, as well as the condition that $\psi(\mathbf{r}_i,\mathbf{r}_i) = 0$ with $i = 1,2$. Equation 1.20 can be written as:

$$\psi(\mathbf{r}_1,\mathbf{r}_2) = \frac{1}{\sqrt{2}}\begin{vmatrix} \phi_1(\mathbf{r}_1) & \phi_1(\mathbf{r}_2) \\ \phi_2(\mathbf{r}_1) & \phi_2(\mathbf{r}_2) \end{vmatrix}. \tag{1.21}$$

This representation of the wavefunction is referred to as the Slater determinant [18]. In the case of more than two electrons, $N > 2$, the normalization prefactor is given by $\frac{1}{\sqrt{N!}}$ and the electron label increases along the horizontal, while the orbital label increases along the vertical of the matrix.

1.1.5 Mean-Field Approximation

As mentioned in Section 1.1.3, there are a few concerns when implementing the independent electron approximation. We discussed the first concern in the previous section, satisfying the Fermi-Dirac statistics. The second issue with the independent electron approximation is that the Coulomb potential is of the same magnitude as the other terms in equation 1.13; thus, it cannot be entirely ignored.

Recall in classical electrostatics, the distribution of an electric charge, $n(\mathbf{r})$, will generate an electrostatic potential, $V_H(\mathbf{r})$, determined by Poisson's equation [14]:

$$\nabla^2 V_H(\mathbf{r}) = -4\pi n(\mathbf{r}), \tag{1.22}$$

with the solution,

$$V_H(\mathbf{r}) = \int d\mathbf{r}' \frac{n(\mathbf{r}')}{|\mathbf{r}-\mathbf{r}'|}. \tag{1.23}$$

Equation 1.23 is referred to as the Hartree potential [19]. Following from the form of the Slater determinant, the electron charge distribution in the independent electron approximation,

$$n(\mathbf{r}) = \sum_i |\phi_i(\mathbf{r})|^2, \tag{1.24}$$

is the sum of the probabilities of finding an electron in each of the occupied states, i. We can improve the representation of the system by including this extra term in $\hat{H}_0(\mathbf{r})$:

$$\left[-\sum_{i=1}^{N} \frac{\nabla_i^2}{2} + V_n(\mathbf{r}) + V_H(\mathbf{r}) \right] \phi_i(\mathbf{r}) = \varepsilon_i \phi_i(\mathbf{r}), \tag{1.25}$$

where $V_n(\mathbf{r})$ is defined as:

$$V_n(\mathbf{r}) = -\sum_i^N \sum_j^M \frac{Z_j}{|\mathbf{r}_i - \mathbf{R}_j|}, \tag{1.26}$$

the Coulomb potential of the nuclei experienced by the electrons. Because the Hartree potential is the average potential experienced by each of the electrons in the independent electron approximation, this approach is referred to as a mean-field approximation.

1.1.6 Indistinguishable Electrons

A final concern that arises within the independent electron approximation is the issue of self-interaction. The single-particle Schrödinger equation for each electron is solved individually and each electron is treated as interacting with every particle in the system. This results in the inclusion of each electrons interaction with itself being considered in the final solution.

1.1.7 Hartree-Fock Equations

The Slater determinant was introduced as a representation of the N-body independent electron wavefunction in Section 1.1.4. In previous sections, however, we noted that the electron interactions cannot be entirely ignored, thus introducing the mean-field approximation. We are able to show that the system can still be represented in the form of a Slater determinant by applying a variational principle. For a given quantum eigenstate, ψ, the energy of the eigenstate is represented as:

$$E = \int d\mathbf{r}_1 ... d\mathbf{r}_N \psi^* \hat{H} \psi = \langle \psi | \hat{H} | \psi \rangle . \tag{1.27}$$

Considering for the time being a system of two electrons, $N = 2$, the corresponding Schrödinger equation is:

$$\left[\hat{H}_0(\mathbf{r}_1) + \hat{H}_0(\mathbf{r}_2) + \frac{1}{|\mathbf{r}_1 - \mathbf{r}_2|} \right] \psi = E \psi, \tag{1.28}$$

where the single-particle Hamiltonian, $\hat{H}_0$ is that defined in equation 1.16. Recall the defi-

nition of the Slater determinant from equation 1.20, which is the solution to the Schrödinger equation for the electronic ground-state energy. Writing the average energy as a function of the normalized wavefunctions:

$$E = \langle \phi_1^* | \hat{H}_0 | \phi_1 \rangle + \langle \phi_2^* | \hat{H}_0 | \phi_2 \rangle + \int d\mathbf{r}_1 d\mathbf{r}_2 \left[\frac{|\phi_1(\mathbf{r}_1)|^2 |\phi_2(\mathbf{r}_2)|^2}{|\mathbf{r}_1 - \mathbf{r}_2|} - \frac{\phi_1^*(\mathbf{r}_1)\phi_2^*(\mathbf{r}_2)\phi_1(\mathbf{r}_2)\phi_2(\mathbf{r}_1)}{|\mathbf{r}_1 - \mathbf{r}_2|} \right]. \tag{1.29}$$

To solve for the ϕ_1 and ϕ_2 that minimize this energy, the following conditions need to be satisfied:

$$\frac{\delta E}{\delta \phi_1} = \frac{\delta E}{\delta \phi_2} = 0. \tag{1.30}$$

We impose normalization and orthogonality of the single-particle wavefunctions using the method of Lagrange multipliers [20]. This involves minimizing an auxiliary function,

$$L[\phi_1, \phi_2, \lambda_{11}, \lambda_{12}, \lambda_{21}, \lambda_{22}] = E[\phi_1, \phi_2] - \sum_{ij} \lambda_{ij} [\langle \phi_i | \phi_j \rangle - \delta_{ij}], \tag{1.31}$$

which is the difference between equation 1.29 and a sum over Lagrange multipliers, λ_{ij}.

In this framework, equation 1.30 is replaced by:

$$\frac{\delta L}{\delta \phi_i^*} = \frac{\partial L}{\partial \lambda_{ij}} = 0, \quad i, j = 0. \tag{1.32}$$

Evaluating these criteria, the following conditions are obtained:

$$\hat{H}_0(\mathbf{r})\phi_1(\mathbf{r}) + \int d\mathbf{r}' \frac{|\phi_2(\mathbf{r}')|^2}{|\mathbf{r}-\mathbf{r}'|}\phi_1(\mathbf{r}) - \int d\mathbf{r}' \frac{\phi_2^*(\mathbf{r}')\phi_2(\mathbf{r})}{|\mathbf{r}-\mathbf{r}'|}\phi_1(\mathbf{r}') = \lambda_{11}\phi_1(\mathbf{r}) + \lambda_{12}\phi_2(\mathbf{r}), \tag{1.33}$$

$$\hat{H}_0(\mathbf{r})\phi_2(\mathbf{r}) + \int d\mathbf{r}' \frac{|\phi_1(\mathbf{r}')|^2}{|\mathbf{r}-\mathbf{r}'|}\phi_2(\mathbf{r}) - \int d\mathbf{r}' \frac{\phi_1^*(\mathbf{r}')\phi_1(\mathbf{r})}{|\mathbf{r}-\mathbf{r}'|}\phi_2(\mathbf{r}') = \lambda_{21}\phi_1(\mathbf{r}) + \lambda_{22}\phi_2(\mathbf{r}), \tag{1.34}$$

$$\int d\mathbf{r}\phi_i^*\phi_j = \delta_{ij}, \quad i,j = 0. \tag{1.35}$$

Recalling the definition of the single-particle Hamiltonian and the Hartree potential, we find:

$$\left[-\frac{\nabla^2}{2} + V_n(\mathbf{r}) + V_H(\mathbf{r})\right]\phi_1(\mathbf{r}) + \int d\mathbf{r}' V_X(\mathbf{r},\mathbf{r}')\phi_1(\mathbf{r}') = \lambda_{11}\phi_1(\mathbf{r}) + \lambda_{12}\phi_2(\mathbf{r}), \tag{1.36}$$

$$\left[-\frac{\nabla^2}{2} + V_n(\mathbf{r}) + V_H(\mathbf{r})\right]\phi_2(\mathbf{r}) + \int d\mathbf{r}' V_X(\mathbf{r},\mathbf{r}')\phi_2(\mathbf{r}') = \lambda_{21}\phi_1(\mathbf{r}) + \lambda_{22}\phi_2(\mathbf{r}), \tag{1.37}$$

where V_X is defined as:

$$V_X(\mathbf{r},\mathbf{r}') = -\sum_j \frac{\phi_j^*(\mathbf{r}')\phi_j(\mathbf{r})}{|\mathbf{r}-\mathbf{r}'|} \tag{1.38}$$

and is called the Fock exchange potential [21], which is a nonlocal potential depending on the wavefunctions of every particle in the system, and therefore complicates the problem

significantly. Because both the Hamiltonian and the Lagrange multipliers are Hermitian, we can introduce a unitary matrix to diagonalize the Lagrange multipliers:

$$S\begin{vmatrix}\lambda_{11} & \lambda_{12}\\ \lambda_{21} & \lambda_{22}\end{vmatrix}S^{-1}=\begin{vmatrix}\varepsilon_1 & 0\\ 0 & \varepsilon_2\end{vmatrix}, \tag{1.39}$$

where $\varepsilon_1, \varepsilon_2$ are real eigenvalues. Additionally, we define a new set of wavefunctions:

$$\psi_i=\sum_j S_{ij}\phi_j. \tag{1.40}$$

Equations 1.36 and 1.37 are rewritten as

$$\left[-\frac{\nabla^2}{2}+V_n(\mathbf{r})+V_H(\mathbf{r})\right]\psi_1(\mathbf{r})+\int d\mathbf{r}'V_X(\mathbf{r},\mathbf{r}')\psi_1(\mathbf{r}')=\varepsilon_1\psi_1(\mathbf{r}), \tag{1.41}$$

$$\left[-\frac{\nabla^2}{2}+V_n(\mathbf{r})+V_H(\mathbf{r})\right]\psi_2(\mathbf{r})+\int d\mathbf{r}'V_X(\mathbf{r},\mathbf{r}')\psi_2(\mathbf{r}')=\varepsilon_2\psi_2(\mathbf{r}). \tag{1.42}$$

It should be noted that within the Hartree-Fock framework, the self-interaction mentioned previously is exactly cancelled.

1.2 Density Functional Theory

The fundamental theorems of density functional theory (DFT) [22] imply that the properties of a many-body system can be represented exactly as a functional of the ground-state

density $n(\mathbf{r})$. In other words the single scalar function, $n(\mathbf{r})$, determines all of the information in the many-body wavefunctions for the ground-state.

1.2.1 Hohenberg-Kohn Theorems

In 1964 Hohenberg and Kohn proved key theorems governing the behavior of the ground-state of an interacting electron gas in an external potential [22]. Here we introduce the Hohenberg-Kohn (HK) theorems and discuss the consequences of these theorems. One of the underlying assertions of the HK theory is that the total ground-state energy of a many-electron system is a functional of the electron density based on the following:

1. In the ground state, the external potential of the nuclei, $V_n(\mathbf{r})$, is a unique functional of the electron density.

2. For any quantum state, $V_n(\mathbf{r})$ uniquely determines the many-body wavefunction.

The second theorem of Hohenberg and Kohn is their variational principle which states that the ground-state density, $n_0(\mathbf{r})$, is exactly the function that minimizes the total energy, $E = E_{HK}[n(\mathbf{r})]$, where

$$E_{HK}[n(\mathbf{r})] = T[n(\mathbf{r})] + E_{internal}[n(\mathbf{r})] + \int d\mathbf{r} V_n(\mathbf{r}) n(\mathbf{r}) + E_N \tag{1.43}$$

$$\equiv F_{HK}[n(\mathbf{r})] + \int d\mathbf{r} V_n(\mathbf{r}) n(\mathbf{r}) + E_N, \tag{1.44}$$

where $T[n(\mathbf{r})]$ is the kinetic energy, $E_{internal}[n(\mathbf{r})]$ is the Coulomb energy, and E_N is the ion-ion interaction energy of the nuclei.

1.2.2 Kohn-Sham Equations

From the HK theorem, we know that the energy of a many-body system in the ground state is a functional of the electron density, however the theorem does not define how this functional is constructed. Expressing the energy as a functional of the electron density, $n(\mathbf{r})$, per the HK theorems:

$$E = E[n(\mathbf{r})] = \int d\mathbf{r} n(\mathbf{r}) V_n(\mathbf{r}) + \langle \psi(\mathbf{r}) | F_{HK}[n(\mathbf{r})] | \psi(\mathbf{r}) \rangle , \tag{1.45}$$

where

$$F_{HK}[n(\mathbf{r})] = T[n(\mathbf{r})] + E_{internal}[n(\mathbf{r})] = -\sum_i \frac{\nabla_i^2}{2} + \frac{1}{2} \sum_{i \neq j} \frac{1}{|\mathbf{r}_i - \mathbf{r}_j|}. \tag{1.46}$$

Clearly, the first term of equation 1.45 is explicitly dependent on the electron density, $n(\mathbf{r})$, however the dependence of the kinetic energy and Coulomb energy are at present only implicit. In their 1965 publication [23], Kohn and Sham split these implicit terms into kinetic and Coulomb energies of independent electrons, as in equation 1.25, with an additional term accounting for exchange and correlation between electrons [15]. Here electronic exchange refers to the interactions between electrons due to their indistinguishability while correlation describes the influence that the movement of one electron has on all other electrons in the system.

$$E = \underbrace{\int d\mathbf{r} n(\mathbf{r}) V_n(\mathbf{r})}_{\text{External potential}} - \underbrace{\sum_i \int d\mathbf{r} \phi_i^*(\mathbf{r}) \frac{\nabla_i^2}{2} \phi_i(\mathbf{r})}_{\text{Kinetic energy}} + \underbrace{\frac{1}{2} \iint d\mathbf{r} d\mathbf{r}' \frac{n(\mathbf{r}) n(\mathbf{r'})}{|\mathbf{r} - \mathbf{r}'|}}_{\text{Hartree energy}} + E_{XC}[n(\mathbf{r})]. \tag{1.47}$$

The extra term, the exchange and correlation energy, represents all of the unknown contributions of the energy encompassed in a single term. We now need to determine how to calculate the ground-state electron density. Kohn and Sham showed that the HK variational principle can be used to derive the following set of coupled single-particle equations:

$$\left[-\frac{\nabla^2}{2}+V_n(\mathbf{r})+V_H(\mathbf{r})+V_{XC}(\mathbf{r})\right]\phi_i(\mathbf{r})=\varepsilon_i\phi_i(\mathbf{r}),\quad n(\mathbf{r})=\sum_i^N|\phi_i(\mathbf{r})|^2 \tag{1.48}$$

and the exchange and correlation potential:

$$V_{XC}(\mathbf{r})=\left.\frac{\delta E_{XC}[n(\mathbf{r})]}{\delta n(\mathbf{r})}\right|_{n(\mathbf{r})}. \tag{1.49}$$

Equations 1.48 are referred to as the Kohn-Sham (KS) equations and form the basis of KS theory [23]. The exchange and correlation energy, E_{XC}, is an exact, universal functional that includes all many-body effects. While in theory there exists a definition of E_{XC} that exactly represents the ground-state energy, this universal functional is at present unknown and must be approximated.

1.2.3 Local Density Approximation

Because the exact exchange and correlation functional is unknown, there is a great deal of effort focused on constructing accurate approximate forms. The simplest approximation of the exchange and correlation functional is the local density approximation (LDA), which depends only on the density at the coordinate where the functional is evaluated. Although

a real material is not adequately represented by a homogeneous electron gas, the premise of the LDA is to partition the volume of the material and consider each infinitesimal volume element to contain a homogeneous electron gas (HEG) because the density of that *localized* volume is varying slowly. To begin, we separate the exchange and correlation energy into two terms representing exchange and correlation independently:

$$E_{XC} = E_X + E_C. \tag{1.50}$$

In LDA, the density is assumed to be locally constant, this typically leads to an underestimated exchange energy and an overestimate of the correlation energy. The LDA is an approximation built off of the idea of the HEG. There exists a gas of N electrons that experience a Coulombic repulsion constrained within a volume, Ω, and the potential of the nuclei is taken to be constant. For the HEG system, we can calculate exactly the exchange energy and the correlation energy can be calculated numerically [24]. The eigenstates and eigenvalues for this system in Hartree units are given by [25]:

$$\psi_{\mathbf{k}}(\mathbf{r}) = \frac{1}{\sqrt{\Omega}} e^{i\mathbf{k}\cdot\mathbf{r}}, \quad \varepsilon_{\mathbf{k}} = \frac{|\mathbf{k}|^2}{2}. \tag{1.51}$$

These solutions are stationary waves, where $\mathbf{k}$ is the wavevector. For the highest occupied state, the value of the eigenvalue is the Fermi energy, ε_F, and the corresponding wavevector is the Fermi wavevector, k_F, where

$$\varepsilon_F = \frac{\mathrm{k}_F^2}{2}, \quad \mathrm{k}_F = (3\pi^2 n)^{\frac{1}{3}}, \tag{1.52}$$

where n is the electron density, $n = N/\Omega$. Now, to determine the exchange energy, we take:

$$E_X = -\sum_{i,j} \int_\Omega d\mathbf{r} \int_\Omega d\mathbf{r}' \frac{\psi_i^*(\mathbf{r})\psi_i(\mathbf{r}')\psi_j^*(\mathbf{r}')\psi_j(\mathbf{r})}{|\mathbf{r}-\mathbf{r}'|}, \tag{1.53}$$

where i and j are indexed over the occupied electronic states and Ω is the volume of the box containing the gas. Plugging in the wavevectors from equation 1.51 and converting our summations to integrals over the continuous functions:

$$E_X = -\frac{1}{(2\pi)^6} \int_{|\mathbf{k}|\leq k_F} d\mathbf{k} \int_{\mathbf{k}'\leq k_F} d\mathbf{k}' \int_\Omega d\mathbf{r} \int_\Omega d\mathbf{r}' \frac{e^{-i(\mathbf{k}-\mathbf{k}')\cdot(\mathbf{r}-\mathbf{r}')}}{|\mathbf{r}-\mathbf{r}'|} \tag{1.54}$$

Implementing integration by substitution, this expression for the homogeneous electron gas exchange energy simplifies to [26]:

$$E_X = -\frac{C}{(2\pi)^6} k_F^4 \Omega = -\frac{3}{4}\left(\frac{3}{\pi}\right)^{1/3} n^{4/3}\Omega. \tag{1.55}$$

Unfortunately, a simple analytic solution to the correlation energy of this system is not known. However, a solution has been found using stochastic numerical methods to sample the many-body Schrödinger equation. In the case of a zero net magnetic moment, the expression for the correlation energy is [24, 27]:

$$E_C = n\Omega \cdot \begin{cases} 0.0311\ln r_s - 0.0480 + 0.002 r_s \ln r_s - 0.0116 r_s & \text{if } r_s < 1, \\ \frac{-0.1423}{1+1.0529\sqrt{r_s}+0.3334 r_s} & \text{if } r_s \geq 1, \end{cases} \tag{1.56}$$

where r_s is the Wigner-Seitz radius, which represents the radius of a sphere whose volume is equal to the volume per electron [28], defined as:

$$\frac{\Omega}{N} = \frac{4\pi}{3} r_s^2 = \frac{1}{n} \tag{1.57}$$

These expressions form the basis for defining the local density approximation used in DFT. In the discretized view of the LDA, each volume element contributes its own exchange-correlation energy:

$$E_{XC} = \int_{\Omega} \frac{E_{XC}^{HEG}[n(\mathbf{r})]}{\Omega} d\mathbf{r}, \quad E_{XC}^{HEG}[n(\mathbf{r})] = E_{X}^{HEG}[n(\mathbf{r})] + E_{C}^{HEG}[n(\mathbf{r})], \tag{1.58}$$

where E_X^{HEG} and E_C^{HEG} correspond to equations 1.55 and 1.56, respectively. Equation 1.58 is the analytic representation of the local density approximation [29].

Given this prescription for solving the exchange-correlation energy, the last step needed to be able to solve the Kohn-Sham equations is to define the exchange-correlation potential, which can be found by using the expression 1.58 in equation 1.49. It is worth noting that the LDA approach to DFT typically results in an exchange potential that is too short-ranged. This is not an exact representation of the *true* exchange-correlation functional and suffers from self-interaction errors.

1.2.4 Self-Consistency

From the previous sections, we now have the tools needed to solve the Kohn-Sham equations (1.48). However, we have demonstrated that the Hartree potential, $\varphi_H(\mathbf{r})$, and the exchange-correlation potential, $V_{XC}(\mathbf{r})$ are both functionals of the electron density, $n(\mathbf{r})$, and thus depend on knowing the density. From the definition of the density in equation 1.48, we know that the density is dependent on the unknown single-particle orbitals, ϕ_i. Within this scheme, each solution to the eigenvectors and eigenvalues implicitly depends on every other solution to the eigenvectors and eigenvalues, therefore they have to be solved self-consistently.

Under this constraint the procedure for solving the Kohn-Sham equations is as follows:

1. Specify the nuclear coordinates of the system such that the nuclear potential, V_n (1.26), can be calculated.

2. Define a first pass guess for the electron density, $n(\mathbf{r})$, which is then used to calculate the initial values of the Hartree, φ_H, and exchange-correlation, V_{XC}, potentials.

3. Numerically solve the Kohn-Sham equations for this initial total potential, V_{tot}, to generate the new wavefunctions.

4. Use these new wavefunctions to construct a better estimate for the electron density and, in turn, the total potential.

5. Repeat this process until the newly calculated density matches the previous density within a desired tolerance.

6. With the final electron density, calculate the total ground-state energy of the system.

1.2.5 Numerical Solutions

There are several approaches to solving the Kohn-Sham equations numerically. Because the Kohn-Sham equations are second-order differential equations, at least two boundary conditions need to be defined in order to solve them. Throughout this paper, the DFT calculations are performed using the software package *Vienna Ab-Initio Simulation Package* (VASP) [30, 31, 32, 33], which utilizes periodic boundary conditions and a planewave representation of the single-particle wavefunctions. For the case of periodic boundary conditions where the computational cell is a cubic volume of side length a, we have:

$$\psi_i(x+a,y,z) = \psi_i(x,y,z), \quad \nabla\psi_i(x+a,y,z) = \nabla\psi_i(x,y,z) \tag{1.59}$$

$$\psi_i(x,y+a,z) = \psi_i(x,y,z), \quad \nabla\psi_i(x,y+a,z) = \nabla\psi_i(x,y,z) \tag{1.60}$$

$$\psi_i(x,y,z+a) = \psi_i(x,y,z), \quad \nabla\psi_i(x,y,z+a) = \nabla\psi_i(x,y,z) \tag{1.61}$$

Within the plane wave basis, the wavefunctions are represented using a Fourier series and solving the Fourier coefficients. The primitive vectors of the reciprocal lattice are defined as [15]:

$$\mathbf{u}_1 = \frac{2\pi}{a}\hat{\mathbf{x}}, \quad \mathbf{u}_2 = \frac{2\pi}{a}\hat{\mathbf{y}}, \quad \mathbf{u}_3 = \frac{2\pi}{a}\hat{\mathbf{z}}, \tag{1.62}$$

where again a is the length of the cubic cell. We define the reciprocal lattice vectors:

$$\mathbf{G} = m_1\mathbf{u}_1 + m_2\mathbf{u}_2 + m_3\mathbf{u}_3, \tag{1.63}$$

where m_1, m_2, m_3 are integer values. The complex exponentials

$$\mathrm{e}^{i\mathbf{G}\cdot\mathbf{r}} \tag{1.64}$$

satisfy the boundary conditions given in equations 1.59, 1.60, 1.61. We can then write the Kohn-Sham orbitals as a linear combination:

$$\psi_i(\mathbf{r}) = \sum_{\mathbf{G}} c_i(\mathbf{G})\mathrm{e}^{i\mathbf{G}\cdot\mathbf{r}}, \tag{1.65}$$

where the sum is over all $\mathbf{G}$ values defined by the integers m_1, m_2, m_3 and $c_i(\mathbf{G})$ are the planewave coefficients. This basis set is in principle infinite, however must be truncated for numerical computation. This truncation is defined by a parameter called the planewave energy cut-off:

$$E_{cut} = \frac{|\mathbf{G}_{max}|^2}{2}, \tag{1.66}$$

where the basis set contains only those functions who satisfy this constraint. The Kohn-Sham equations for the system are then written as:

$$\frac{|\mathbf{G}|^2}{2} c_i(\mathbf{G}) + \sum_{\mathbf{G}'} v_{tot}(\mathbf{G} - \mathbf{G}') c_i(\mathbf{G}') = \varepsilon_i c_i(\mathbf{G}), \tag{1.67}$$

$$V_{tot}(\mathbf{G}) = \frac{1}{a^3} \int d\mathbf{r}\, \mathrm{e}^{-i\mathbf{G}\cdot\mathbf{r}} V_{tot}(\mathbf{r}) \tag{1.68}$$

1.2.6 Pseudopotential Approximation

In many cases, particularly when simulating high-Z materials, numerical calculations quickly become too computationally intensive for present day computational capacity. In these scenarios it is often advantageous to explicitly consider only the valence electrons of an atom. This is done by introducing the idea of a pseudopotential [29, 34]. The underlying notion within this representation is that the core electrons are tightly bound to the nucleus and can be considered chemically inert. This is done by modifying the nuclear potential such that it satisfies the following conditions:

1. Outside the region that is being "pseudized," the modified potential matches the original Kohn-Sham potential which accounts for all electrons.

2. Inside the region that is being "pseudized," the modified potential yields the exact same eigenvalue solution to the Kohn-Sham equations as the pseudo-wavefunction.

1.2.7 Generalized Gradient Approximation

There has been significant success in characterizing materials using the LDA exchange-correlation functional, oftentimes reliably calculating properties of systems that are very far removed from the homogeneous electron gas. However, there exist situations were a more accurate description of the exchange and correlation energies is needed. The next step forward in accuracy has been through the development of generalized-gradient approximations (GGA) [29]. These functionals are the first departure from an entirely localized reliance on the density, characterized by their dependence on the first-order gradient of the density, ∇n, as well as n at each point. In many cases, GGA functionals surpass the LDA in performance, however this is not a universal trait.

To define the gradient expansion of the exchange-correlation functional, it is convenient to consider the exchange-correlation energy in terms of that for the HEG system [35],

$$E_{XC} = \int_{\Omega} E_X^{HEG}[n(\mathbf{r})] F_{XC}[n(\mathbf{r}), \nabla n(\mathbf{r})] n(\mathbf{r}) d\mathbf{r}. \tag{1.69}$$

Throughout this dissertation, the particular GGA described by Perdew, Burke, and Ernzerhof (PBE) [36] is used. The PBE exchange and correlation functional was created to preserve the features of the LDA while also including the most energetically important

features of gradient-corrected nonlocality. PBE is a non-empirical functional thus it depends only on the rules of quantum mechanics with special limiting conditions, such as the correct asymptotic behavior for large distances and the correct description of the uniform electron gas. PBE is considered widely applicable to many different systems while also providing computational efficiency making it a popular choice among GGAs. PBE is an attractive choice where dispersion interactions are not dominant.

1.3 Molecular Dynamics

Molecular dynamics (MD) is a general computer simulation approach to analyze the physical movements of atoms and molecules. In this dissertation we are using density functional theory based molecular dynamics (DFTMD). In this framework, the motion of the electrons and the corresponding energies and forces are determined using DFT, described in Section 1.2.4. The motion of the ions are then solved classically using Newton's equations. This process is then repeated for the number of desired timesteps.

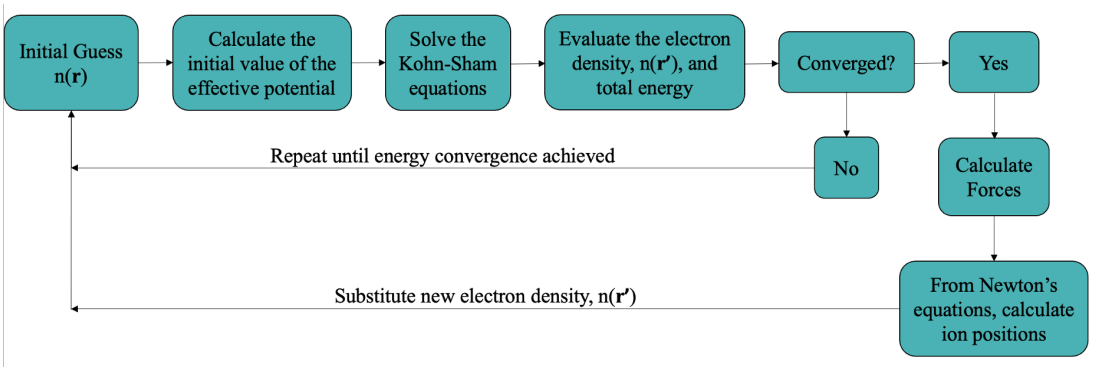

Figure 1.1: Flowchart depicting the procedure for solving for one timestep in a molecular dynamics simulation implementing DFT. The process of converging the energy is described in section 1.2.4.

Chapter 2

Motivations

Liquid-vapor coexistence in materials is a phenomenon that is encountered every day, with the entirety of our day-to-day lives existing within the liquid-vapor coexistence region of water [37, 38]. In addition to the commonly observed water liquid-vapor phases, understanding coexistence is crucial for many industrial and scientific applications. The process of decaffeinating such substances as coffee and tea utilizes supercritical CO_2 to dissolve and remove caffeine [39]. In contrast to using chemical solvents, this method of decaffeination is used to minimally impact the original flavors. Another example of the importance of characterizing liquid-vapor coexistence within industrial processes is the process of refining crude oil. Through petroleum distillation, crude oil is separated into different fractions of gasoline, kerosene, and diesel based on the boiling points of the components [40].

Many topics within scientific research are also concerned with understanding liquid-vapor coexistence and critical behavior. Within the field of astrophysics, the accretion of planetary bodies and giant impact events result in the creation of considerable amounts

of supercritical fluids [41]. For shock experiments involving dynamic compression, materials may intersect the liquid-vapor phase boundary at late times as they isentropically decompress [8].

Typically the temperatures and pressures at the liquid-vapor critical point for metals are extremely high, making experimental investigation incredibly difficult. Direct measurements and characterization of the critical point are only available for metals with low melting points, such as mercury [42, 43]. This has resulted in a heavy reliance on theoretical methods of investigating material behaviors in this regime. In this dissertation, we have characterized the liquid-vapor coexistence and critical behavior of platinum using density functional theory. Platinum is frequently used as a high pressure material standard in shock compression experiments [44, 9]. At the Z Pulsed Power facility at Sandia National Laboratories platinum is used as a high-impedance impactor in flyer plate shock compression experiments [8]. Despite its use as a standard, current estimates of the liquid-vapor critical point of platinum are highly unconstrained, spanning approximately 7000 K and 2 g/cm^3 [1, 2, 3, 4, 5, 6].

Chapter 3

Liquid-Vapor Coexistence of Platinum from *Ab-initio* Simulations

The contents of this chapter have been submitted as part of *Meghan K. Lentz, Michael P. Desjarlais, and Joshua P. Townsend; Liquid-Vapor Coexistence of Platinum from Ab-initio Simulations. J. Chem. Phys. (in revision).* Minor edits within this dissertation have been made to clarify the text.

3.1 Abstract

Platinum is a standard material for high pressure experiments, yet estimates of the liquid-vapor critical temperature and density span nearly 7000 K and 2 g/cm^3. Here we present the results of the first systematic investigation of liquid-vapor coexistence and critical behavior of platinum using density functional theory-based molecular dynamics. We ob-

tained critical point parameters and an estimate of the liquid-vapor phase boundary from a fit to a generalized virial equation of state model and subsequent Maxwell construction on isotherms below the critical temperature. We performed this analysis on different sized systems in order to quantify finite size effects. We extrapolated our results to the thermodynamic limit and found a critical point of $\rho_c = 4.18 \pm 0.09$ g/cm^3, $T_c = 8120 \pm 60$ K, and $P_c = 5.56 \pm 0.50$ kbar. Our predicted phase boundary agrees well with recent experiments measuring the liquid side of the Pt vapordome, demonstrating significant improvement in the phase diagram in this region.

3.2 Introduction

Platinum (Pt) is a metal with a high melting point whose face-centered cubic crystal does not display any experimentally observed solid-solid phase changes up to its melt [45] and is predicted to remain stable up to at least 800 GPa [46, 44, 47]. Due to these properties and others, platinum is frequently used as a material standard, in high-pressure and shock compression physics. Pt is also used as a high-impedance impactor in flyer plate shock experiments [44, 48], which may enter the liquid-vapor coexistence region upon release. Despite continued interest in the high pressure and temperature phase diagram, the properties of the liquid-vapor region remain poorly understood. Clarity in this region of the phase diagram spanning liquid and vapor states is hindered due to the experimental challenges that come with confining high temperature liquid and vapor.

Indeed, previous estimates of the critical point typically rely on extrapolations from low temperature measurements employing exploding wire and pulsed heating techniques [5, 3]. In contrast to the described low temperature extrapolations, previous computational

studies have relied on classical interatomic potentials trained from low-pressure data or simplified equation of state (EOS) models from which a critical point can be directly calculated [6, 2, 4, 1, 49, 50]. Taken together, the estimates of the critical temperature, T_c, span about 7000 K and estimates of the critical density, ρ_c, span about 2.00 g/cm^3, shown in Figure 3.1. To our knowledge, there have been no *ab initio* studies to date and the need for such calculations in this region has been noted by Elkin *et al.* [49].

Ab-initio techniques such as density functional theory based molecular dynamics (DFTMD) do not rely on experimental input and thus offer, in principle, an independent method to investigate critical behavior. Such methods have been used previously to study the critical behavior and phase diagrams of a wide variety of systems oftentimes using different approaches [51, 52, 53, 54, 55]. A universal concern with atomistic simulations in the coexistence region are the influences of finite size and time effects, which, in addition to the usual DFT approximations, may result in significant bias in the results.

In this study we present a systematic investigation of the properties of platinum in the liquid-vapor coexistence region from DFTMD calculations. To better understand the nature of microscopic liquid and vapor, we first examine the MD trajectories and speciation of the system around the coexistence region. We then compare estimates of the critical point and liquid-vapor phase boundary obtained using three different sized systems fitting the density, pressure, and temperature states to a general virial EOS in order to estimate finite size effects. We find a critical point whose critical temperature is generally lower than most of the previously reported data seen in Figure 3.1. We offer, to our knowledge, the first *ab initio* characterization of the liquid-vapor phase boundary. Additionally, we find exceptional agreement with recent experimental measurements done of the liquid side of the phase boundary [8].

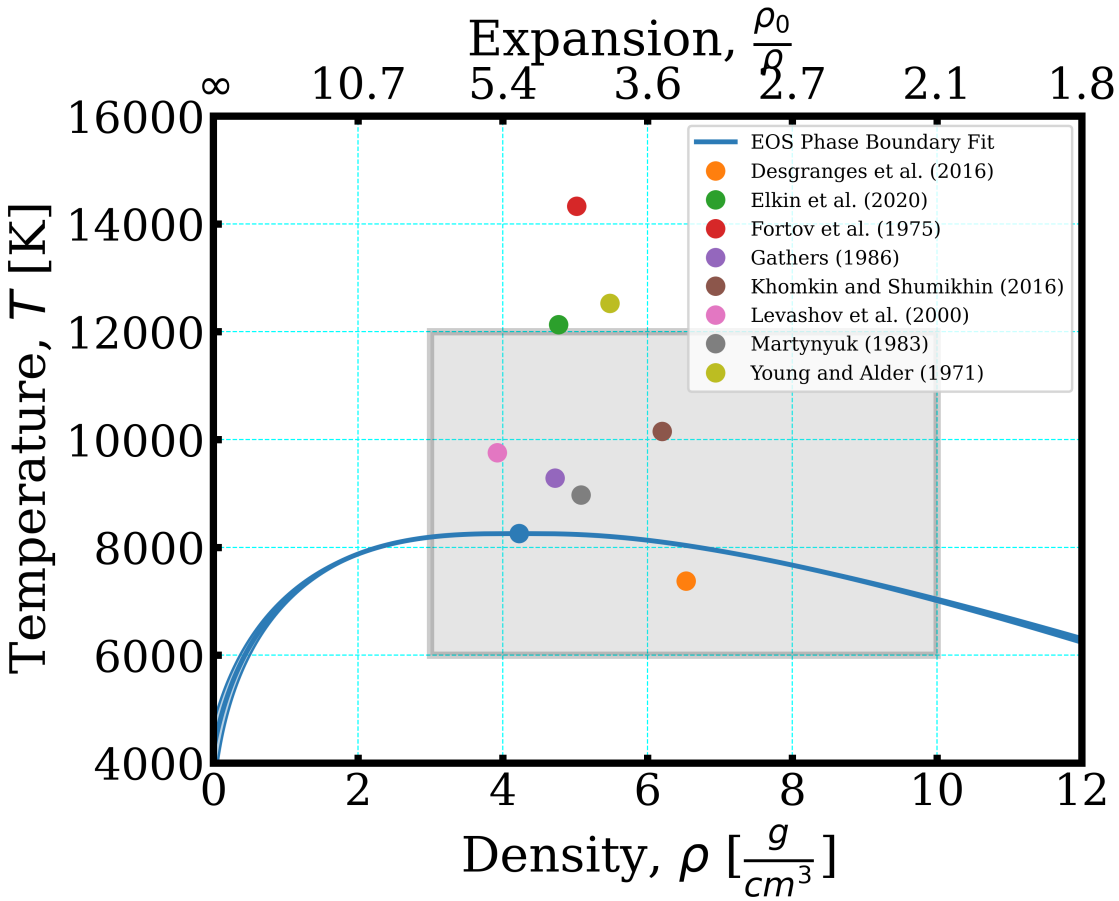

Figure 3.1: The Pt critical point and liquid-vapor phase boundary calculated from a Maxwell construction of a 256-atom system fit to an EOS are shown in blue. The various colored individual points indicate previously calculated critical points [1, 2, 3, 4, 5, 6]. The gray shaded region is the region of phase space that has been simulated using DFTMD.

3.3 Molecular Dynamics Calculations

DFTMD calculations were performed with the Vienna *ab initio* simulation package (VASP) [30, 31, 32, 33], an implementation of Kohn-Sham DFT [22, 23] using a planewave basis

and periodic boundary conditions. A platinum projector augmented wave (PAW) pseudopotential [56] with a $5d^9 6s^1$ valence configuration was used and the energy plane wave cutoff was set to 700 eV. The exchange-correlation energy was computed with the Perdew-Burke-Ernzerhof (PBE) generalized gradient approximation [36]. All simulations were conducted within the NVT ensemble with a velocity scaling thermostat. The Brillouin zone was sampled at the Γ point and the electronic occupations were populated using a Fermi-Dirac distribution according to the Mermin finite temperature formulation of DFT [57, 58, 54, 48]. Calculations were performed over a grid of temperatures, 6000-12000 K, densities, 3.00-10.00 g/cm^3, and particle number, 32, 108, and 256. Each simulation was initialized from an fcc crystal and run for approximately 10000 1-fs time steps and checked for equilibrated pressures.

The trajectories obtained from the MD simulations show a rich variety of dynamical behavior. At higher densities we have observed by visual inspection a homogeneous fluid phase, while at lower densities and temperatures we observed phenomena such as droplet formation and evaporation, as well as ephemeral bubbles and foams. The use of a plane-wave basis limits the minimum density we can study because the size of the basis scales with the cell volume. Thus our lowest density simulations (3 g/cm^3) do not lie entirely outside the coexistence region (note the grey shaded box in Figure 3.1).

Figure 3.2 shows the distribution of platinum clusters for selected density, temperature points. In this analysis, an atom is defined to be part of a cluster if there is a neighboring atom within the value of the first minimum of the radial distribution function (RDF). For those densities studied, the 6000 K isotherm exists almost entirely inside the vapor dome. This is supported by the lack of any intermediate cluster sizes; with the entire population being made up of very large (liquid) clusters or clusters with only a few platinum atoms (vapor) consistent with a sub-critical two phase system. Completely outside of the coexis-

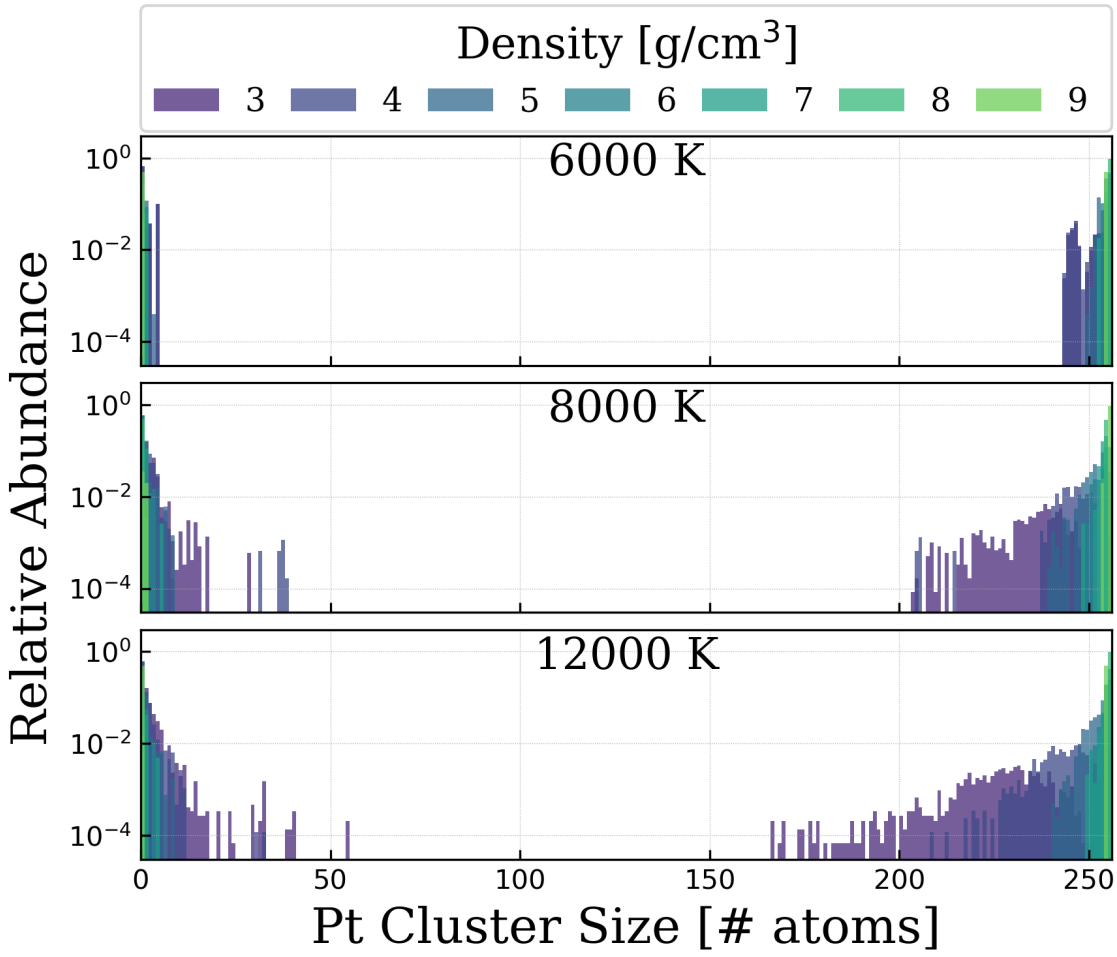

Figure 3.2: Platinum speciation cluster size along three different isotherms: 6000 K, 8000 K, and 12000 K for the range of calculated densities.

tence region, along the 12000 K isotherm, these well defined phases seemingly disappear and we see clusters of many different sizes present throughout the simulation, consistent with a supercritical fluid. The intermediary 8000 K isotherm is near criticality, with some densities existing inside the coexistence region and some outside. This is evident by the population of Pt clusters predominantly being made up of very large and very small clus-

ters, with the additional presence of a small number of intermediate sized clusters for the lowest densities.

3.4 Results

3.4.1 Equation of State Model

We used a generalized virial EOS [54] to represent the pressure, P, in the coexistence region:

$$P(n,T) = k_B T n + (a_0 + a_1 k_B T) n^2 + (b_0 + b_1 k_B T) n^3 \tag{3.1}$$

where n is the atomic number density (N/V) in units of $1/\text{Å}^3$, k_B is the Boltzmann constant, T the temperature, where $k_B T$ is in units of eV, and a_0, a_1, b_0, b_1 are obtained from a least-squared fit to the DFTMD data. We find $a_0 = -72.8 \pm 7.1$, $a_1 = 26.2 \pm 8.9$, $b_0 = 594 \pm 259$, and $b_1 = 1110 \pm 326$, with the following correlation matrix for the vector of fit coefficients $[a_0, a_1, b_0, b_1]$:

$$\begin{bmatrix} 1.00 & -0.98 & -0.99 & 0.96 \\ -0.98 & 1.00 & 0.96 & -0.99 \\ -0.99 & 0.96 & 1.00 & -0.98 \\ 0.96 & -0.99 & -0.98 & 1.00 \end{bmatrix} \tag{3.2}$$

We note that due to the large correlations between EOS parameters in our model, the uncertainty in, for example, the liquid density at 6000 K is approximately 0.4 g/cm^3 (3%

relative error). The EOS obtained from the 256 atom simulations is shown in Figure 3.3. Regardless of the underlying EOS model, the critical point satisfies:

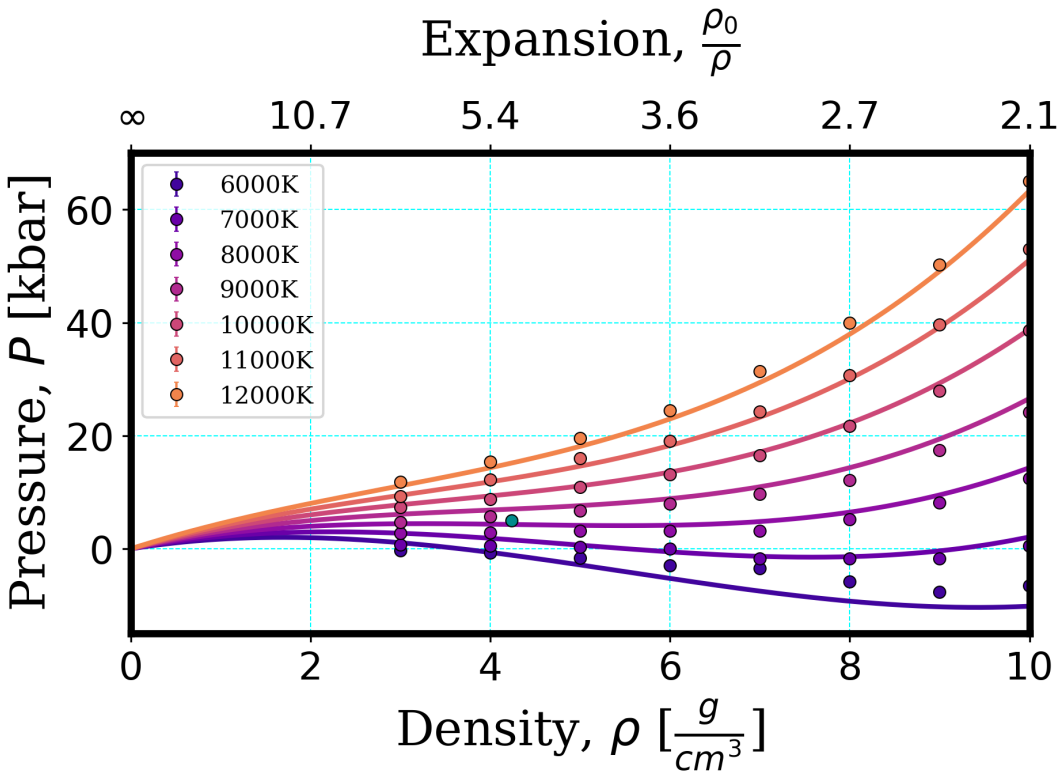

Figure 3.3: EOS fit (lines) to the DFTMD results (points) for the 256-atom supercell with the critical point estimation (blue circle). The top axis represents the expansion of the system, where $\rho_0 = 21.45$ g/cm^3 is the density of Pt at ambient. Note we have converted number density to mass density using the atomic mass of platinum.

$$\left(\frac{\partial P}{\partial n}\right)_{T=T_c} = \left(\frac{\partial^2 P}{\partial n^2}\right)_{T=T_c} = 0. \tag{3.3}$$

The critical density, temperature, and pressure for our chosen EOS are then simple algebraic expressions in the EOS parameters:

$$T_c = \frac{-B \pm \sqrt{B^2 - 4AC}}{2A} \tag{3.4}$$

$$n_c = -\frac{1}{3}\frac{a_0 + a_1 k_B T_c}{b_0 + b_1 k_B T_c} \tag{3.5}$$

$$P_c = P(n_c, T_c) \tag{3.6}$$

where $A = b_1 - \frac{1}{3}a_1^2$, $B = b_0 - \frac{2}{3}a_0 a_1$, and $C = -\frac{1}{3}a_0^2$.

The isotherms obtained from the EOS model clearly show a region of instability at low temperature where $(\partial P/\partial n)_T < 0$. Applying the familiar Maxwell equal area rule [59] to isotherms in this region gives a bound on the metastable and unstable regions which provide an estimate of the liquid-vapor phase boundary. From these points in combination with the critical point we then calculated the binodal coexistence curve by fitting these points to the Wegner expansion: [60]

$$\rho_v = \rho_c - \frac{1}{2}\left(C_1 x^{\beta} + C_2 x^{\beta+\Delta}\right) + C_3 x \tag{3.7}$$

$$\rho_l = \rho_c + \frac{1}{2}\left(C_1 x^{\beta} + C_2 x^{\beta+\Delta}\right) + C_3 x \tag{3.8}$$

where ρ is the mass density, $\rho = mn$, $x = \left(1 - T/T_c\right)$ and the (fixed) critical exponents correspond to the 3D Ising model $\Delta = 0.5$ and $\beta = 0.325$ [61]. Repeating this approach, we have calculated a series of critical points for Pt for each of the different sized systems, shown in Table 3.1. The values of parameters C_1, C_2, and C_3 for the 256-atom system are $C_1 = 11.16 \pm 0.12$, $C_2 = 14.39 \pm 0.43$, and $C_3 = 8.56 \pm 0.02$, with the following correlation matrix for the vector $[C_1, C_2, C_3]$:

$$\begin{bmatrix} 1.00 & -0.84 & -0.71 \\ -0.84 & 1.00 & 0.98 \\ -0.71 & 0.98 & 1.00 \end{bmatrix} \tag{3.9}$$

At the low density limit, the EOS model is dominated by the ideal gas behavior. We investigated the sensitivity of the critical point parameters to the choice of density and temperature data and found that excluding the 3, 4, 5, 6, and 7 g/cm^3 isochores from the EOS model fit resulted in a critical density that is approximately 0.1 g/cm^3 different and a critical temperature with a less than 100 K difference. The critical point comparison for the various data ranges is shown in Figure 3.4. The EOS parameters are most sensitive to the highest density isochores due to the constraint of the low density ideal gas limit. This strong dependence of the shape of the EOS fit on the ideal gas form is also the cause for the significant correlation between parameters evident in Equation 3.2.

We found that the curvature of the isotherms in the coexistence region decreased with system size, as expected [62]. In order to quantify the sensitivity of the critical point parameters to the system size, we performed a finite size extrapolation of the critical density, temperature, and pressure to the thermodynamic limit using known scaling laws [7], shown in Figure 3.5. We obtain: $\rho_c^{TDL} = 4.18 \pm 0.09$ g/cm^3, $T_c^{TDL} = 8120 \pm 60$ K, and $P_c^{TDL} = 5.56 \pm 0.50$ kbar. The critical point calculated for the 256 atom supercell is within 2% of the critical point estimate at the thermodynamic limit (Table 3.1). We concluded that the finite size effects for the critical point of the 256 atom system are small, from this we assumed the phase boundary calculated for the 256 atom system is reasonably well converged with respect to system size.

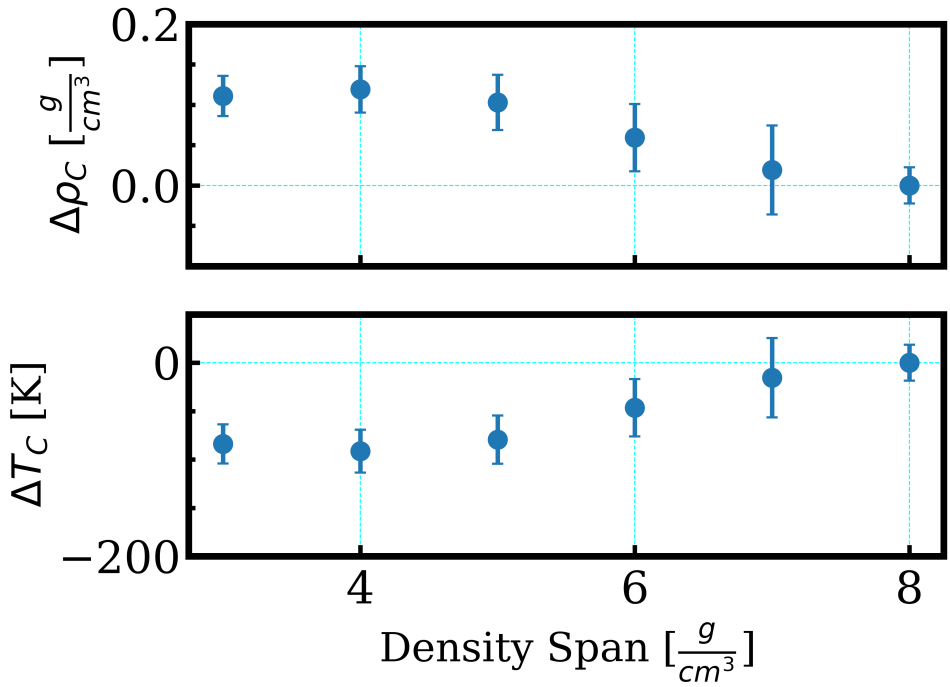

Figure 3.4: Critical point comparison excluding low density isochores in the EOS model fit. The reference point at y=0 corresponds to the full range of data, including 3.00-10.00 g/cm^3 isochores. We compare the change in critical parameters for as few as 7.00-10.00 g/cm^3 isochores, corresponding to a density span of 3 g/cm^3.

3.5 Summary

In summary, we have carried out a systematic investigation of the properties of platinum in the liquid-vapor coexistence region and provided an improved estimate of the critical point: $\rho_c = 4.18 \pm 0.09$ g/cm^3, $T_c = 8120 \pm 60$ K, and $P_c = 5.56 \pm 0.50$ kbar. We found that the critical point obtained from an EOS model fit to the 256-atom DFTMD data was within 2% of the extrapolated value at the thermodynamic limit.

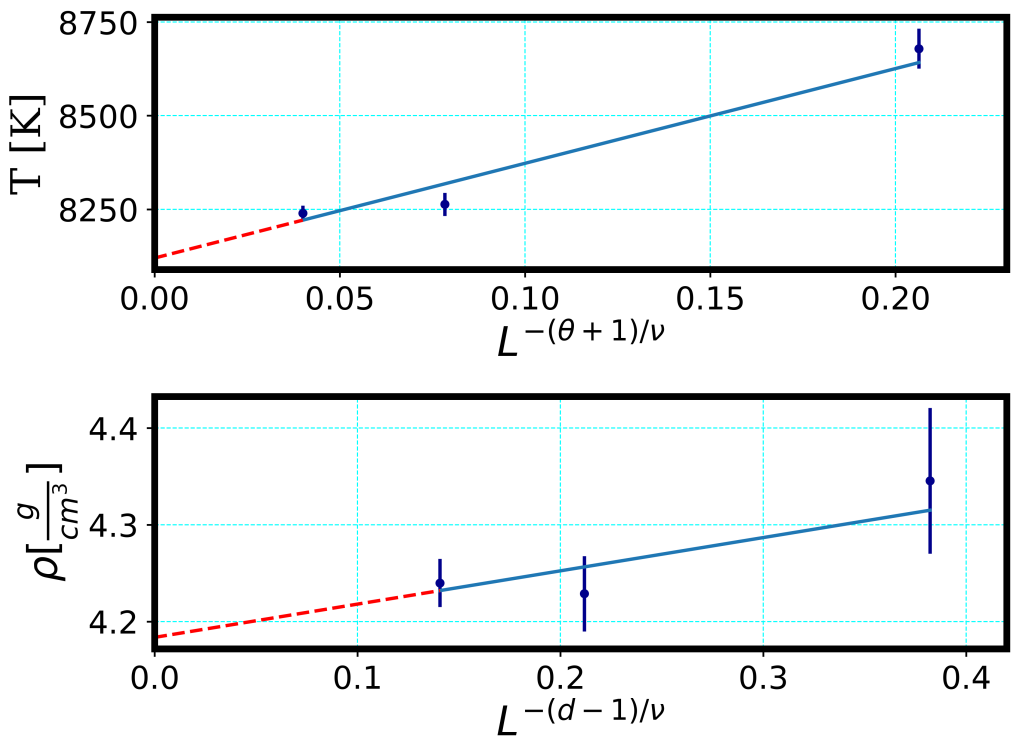

Figure 3.5: Extrapolation of the critical point obtained from DFTMD to the thermodynamic limit using the finite-size scaling technique described in Wilding (1995) [7]. Here, L is the length, with dimension $d = 3$, $\theta = 0.54$ and $\nu = 0.629$.

N	ρ_c	T_c	P_c
[atoms]	[g/cm^3]	[K]	[kbar]
32	4.34 ± 0.08	8680 ± 50	9.59 ± 0.74
108	4.23 ± 0.04	8260 ± 30	6.54 ± 0.26
256	4.24 ± 0.03	8240 ± 20	6.44 ± 0.19
TDL	4.18 ± 0.09	8120 ± 60	5.56 ± 0.50

Table 3.1: Critical points calculated for the 32, 108, and 256 atom systems. Also shown is the critical point at the thermodynamic limit (TDL).

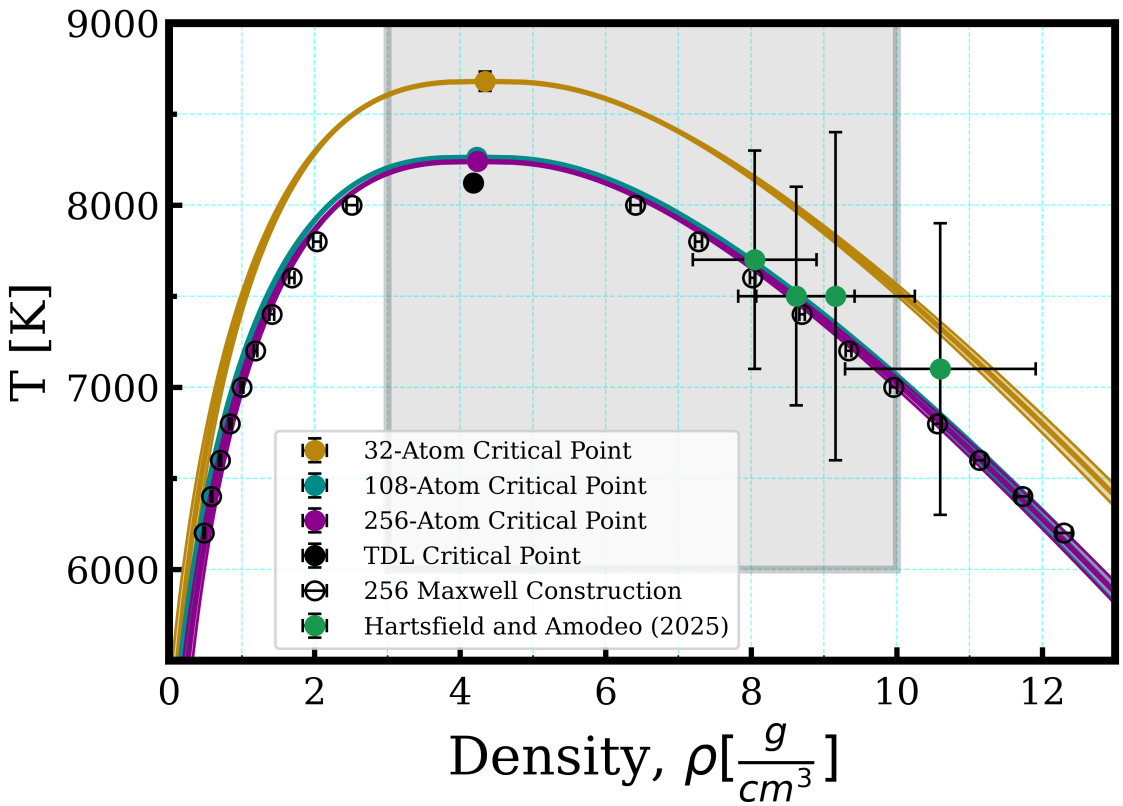

Figure 3.6: Phase diagram for the different sized Pt systems. The 256-atom EOS Maxwell construction is shown with the black circles. The TDL extrapolated critical point is shown by the filled in black point. The region calculated with DFTMD is shaded grey. Also shown in green is experimental Z machine data [8].

Our results suggest a critical point that is lower in density and temperature compared to most previous estimates. Previous estimates of the critical point are based on indirect measurements [3, 5] extrapolated from low-temperature experiments and simplified theoretical models [1, 49, 2, 4, 50, 6] derived from low-pressure data. Recent measurements of the liquid side of the liquid-vapor phase boundary obtained from shock release experiments on the Z machine at Sandia National Laboratories [8] agree very well with

our calculated phase boundary, shown in Figure 3.6, and therefore lend confidence to the results presented here.

While we have accounted for the influence of finite size effects, there exist other sources of possible bias: such as the choice of exchange-correlation functional and the method used to determine the critical parameters. There exist additional *ab initio* approaches of characterizing the liquid-vapor coexistence region [63, 64, 65]. The sensitivity of the critical point to the calculation technique will be the focus of a future study.

3.6 Conflict of Interest

The authors have no conflicts to disclose.

3.7 Data Availability

The data that support the findings of this study are available from the corresponding author upon reasonable request.

3.8 Acknowledgements

The authors would like to thank Kyle Cochrane, Amanda Dumi, and Cody Melton for many helpful discussions. Sandia National Laboratories is a multi-mission laboratory managed and operated by National Technology & Engineering Solutions of Sandia, LLC

(NTESS), a wholly owned subsidiary of Honeywell International Inc., for the U.S. Department of Energy's National Nuclear Security Administration (DOE/NNSA) under contract DE-NA0003525. This written work is authored by an employee of NTESS. The employee, not NTESS, owns the right, title and interest in and to the written work and is responsible for its contents. Any subjective views or opinions that might be expressed in the written work do not necessarily represent the views of the U.S. Government. The publisher acknowledges that the U.S. Government retains a non-exclusive, paid-up, irrevocable, world-wide license to publish or reproduce the published form of this written work or allow others to do so, for U.S. Government purposes. The DOE will provide public access to results of federally sponsored research in accordance with the DOE Public Access Plan.

Chapter 4

Quantifying Shape Effects on Estimates of the Liquid-Vapor Interface of Platinum

The contents of this chapter have been written as part of *Meghan K. Lentz, Michael P. Desjarlais, and Joshua P. Townsend; Quantifying Shape Effects on Estimates of the Liquid-Vapor Interface of Platinum. J. Chem. Phys. (in preparation).*

4.1 Abstract

Understanding the physical properties of materials in the liquid-vapor coexistence region is crucial for a variety of applications, including material design, energy storage, and understanding fundamental thermodynamic processes. However, the liquid-vapor coexistence

region is often oversimplified, typically relying on extrapolations from low-temperature data that may not capture the behaviors of phase transitions in this regime. In this chapter, we conducted density functional theory molecular dynamics (DFTMD) simulations of platinum along a 5.00 g/cm^3 isochore, exploring a range of temperatures to characterize the liquid-vapor phase boundary. From the DFTMD we analyzed particle trajectories and applied an instantaneous interface calculation, leading to the determination of the critical point and the liquid-vapor phase boundary. We investigated the sensitivity of the critical point and phase boundary to shape effects arising from complex geometries, which are often encountered in real-world applications. To validate our results, we compared the calculated critical parameters with previously published data obtained through an alternative, independent technique for characterizing the liquid-vapor region of platinum. We find that the calculated liquid-vapor phase boundary is highly sensitive to the geometry of the interface.

4.2 Introduction

Liquid-vapor coexistence is a ubiquitous phenomenon in nature. Indeed, common human experience takes place entirely within the liquid-vapor coexistence region of water [37, 38]. Generally understanding liquid-vapor coexistence is important for a variety of scientific and industrial applications. For example, many industrial chemical processes rely on the ability to vaporize and distill materials [39, 40]. Additionally, many astrophysical processes rely on material behaviors under extreme conditions; within planetary accretion copious supercritical fluid is created through giant impact events [41]. Similarly, in dynamic compression experiments when materials isentropically decompress they may intersect the liquid-vapor coexistence region [8] at late-times. There are many practical

challenges associated with investigating these regimes for transition metals in particular. Due to their high melting temperatures, experimental data is oftentimes difficult to obtain due to the difficulties of confining high temperature liquid and vapor metals [42]. For example, prior studies on platinum (Pt) liquid-vapor coexistence show a large uncertainty in the location of the liquid-vapor critical point [1, 2, 3, 4, 5, 6, 9].

Due to the difficulties of experiments, there is a need for theoretical approaches to produce highly accurate phase diagrams. A common starting point for understanding critical behavior of fluids is the Van der Waals equation of state (EOS). Below the critical temperature, isotherms inside of the liquid-vapor coexistence region show what are referred to as Van der Waals (vdW) loops, where there is a portion of the isotherm such that the pressure increases with increasing volume, representing an unstable state [66]. The Maxwell construction, described in Figure 4.4, is a method for addressing this instability [67] and identifying the liquid-vapor phase boundary. Due to the finite size and time of molecular dynamics calculations there is the appearance of vdW-like loops on isotherms inside the liquid-vapor coexistence region due in part to oscillations between metastable states [62, 64, 68, 69].

Ab initio techniques such as density functional theory based molecular dynamics (DFTMD) offer the possibility of improved accuracy over simple classical potentials, but biases due to finite size remain [9, 51, 52, 53, 54, 55, 64, 65, 69]. Despite the use of these methods in the past, the influence of potential sources of bias is typically omitted, oftentimes due to the significant expense of the simulations. Without a proper understanding of the sources of bias and their influence in the resulting estimates of material properties confidence is limited. Due to the known phenomenon of a divergence in the correlation length for systems near the liquid-vapor critical point in the thermodynamic limit, length scales of all magnitude are relevant in this regime, leading to typically large sensitivities

to finite size effects.

This chapter is a follow up to the previous chapter on the liquid-vapor coexistence of Pt found from a fit to a generalized equation of state (EOS). We conducted DFTMD simulations within the liquid-vapor coexistence region of platinum. We compare estimates of the critical point and liquid-vapor phase boundary for different simulation geometries obtained from a partitioning of the system into regions of liquid and vapor according to an instantaneous interface calculation [65]. Previous studies have predicted liquid-vapor phase behavior using the method of instantaneous interface calculations when considering a slab-like geometry [65, 53]. While it is postulated that this approach is robustly applicable to arbitrary geometries [65], we find that the geometry of the system is immensely important with respect to the systems ability to represent liquid-vapor coexistence at the thermodynamic limit. This is in agreement with previous work in which it was shown that the growth of the vdW-like loops is proportional to the surface area of the two-phase interface [69].

4.3 Methods

4.3.1 Molecular Dynamics Calculations

Density functional theory calculations [22, 23] were performed using the Vienna *ab initio* simulation package (VASP) [30, 31, 32, 33] with the same initial conditions as described in [9], using a planewave basis and periodic boundary conditions. A 10 e^- platinum pseudopotential [56] was used and the energy plane wave cutoff was set to 700 eV. The exchange-correlation energy was computed with the Perdew-Burke-Ernzerhof (PBE) gen-

eralized gradient approximation [36] and all simulations were conducted within the NVT ensemble with a velocity scaling thermostat. The Brillouin zone was sampled at the Γ point and the electronic occupations were populated using a Fermi-Dirac distribution according to the Mermin finite temperature formulation of DFT [48, 54, 57, 58]. Calculations were performed along a 5.00 g/cm^3 isochore for a range of temperatures, 4000-8000 K, with 500 K increments. Each simulation was checked for equilibrated pressures. We looked at two different sized systems, 108- and 256-atoms, and two atomic configurations, a slab of liquid continuous in two dimensions surrounded by vapor and a heterogeneous mixture of vapor pockets and liquid droplets inside of a cubic volume. We have noted that the slab of liquid loosely resembles a french fry, while the cubic volume resembles a block of Swiss cheese. Throughout this chapter we will be referring to the systems as the "french fry" and "Swiss cheese" geometries.

4.3.2 Instantaneous Liquid Interface Approximation

To investigate coexistence we have followed the instantaneous interface calculation described in Willard and Chandler (2010) [65]. In this scheme, we coarse-grain the mass distribution inside the cell by convolving the position of every particle with a normalized Gaussian. After coarse-graining we obtained a time-dependent density field, $\tilde{n}$, given by:

$$\tilde{n}(\mathbf{r},t) = (2\pi\xi^2)^{-\frac{3}{2}} \sum_i^N e^{\frac{-|\mathbf{r}-\mathbf{r}_i(t)|^2}{2\xi^2}} \tag{4.1}$$

where $\mathbf{r}_i(t)$ is the position of the i^{th} particle at time t and ξ is the coarse-graining length. We have defined ξ to be the weighted average of all distances covered by the first peak in the RDF, $g(r)$, shown in figure 4.1: [70]

$$\xi \equiv \frac{\int_0^{r_{min}} rg(r)dr}{\int_0^{r_{min}} g(r)dr}. \tag{4.2}$$

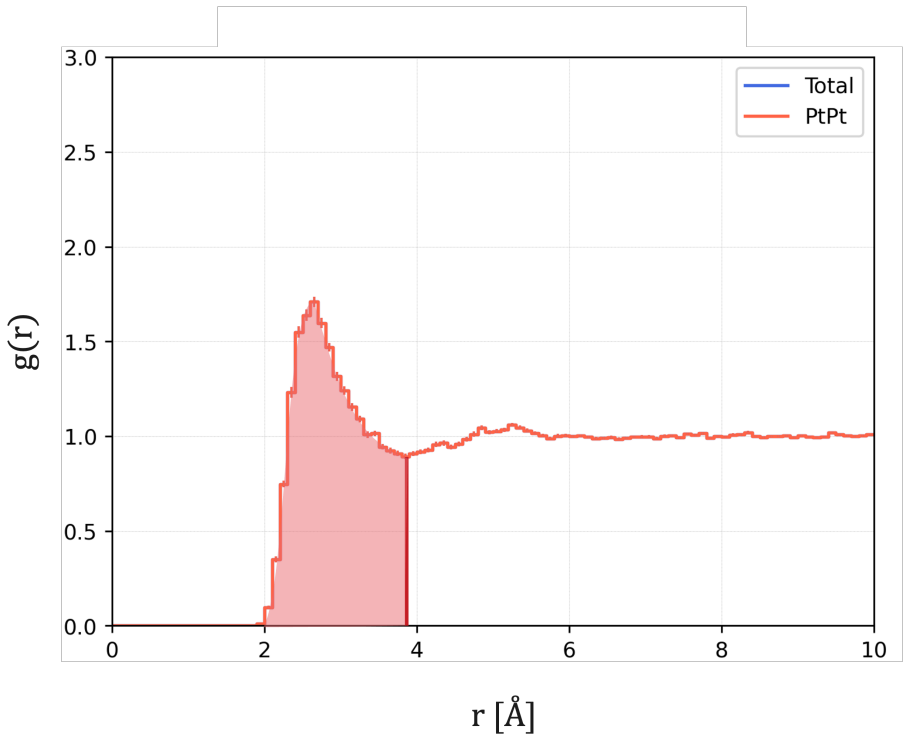

Figure 4.1: Schematic showing the value used, the area of the red shaded region, for calculating the coarse-graining length for the instantaneous interface calculations.

Within this coarse-grained density field, regions of high density are liquid and regions of low density are vapor. A particle is defined to belong to the liquid phase above the predetermined cut-off density which we have chosen to be the average density of the field, $\tilde{n}_i(\mathbf{r},t) \geq \tilde{n}_{avg}$. Similarly, the particle is in the vapor phase below this cut-off, $\tilde{n}_i(\mathbf{r},t) < \tilde{n}_{avg}$.

Once the particles have been partitioned into the separate phases the number of atoms and volume of the liquid phase can be calculated using:

$$N_l = \int_{\Omega_l} dxdydz \sum_i^N \delta(x-x_i)\delta(y-y_i)\delta(z-z_i), \tag{4.3}$$

$$V_l = \int_{\Omega_l} dxdydz, \tag{4.4}$$

where N is the total number of atoms in the system and Ω_l is the liquid region where $n \geq \tilde{n}_{avg}$. Similarly, Ω_v corresponds to the region where $n < \tilde{n}_{avg}$ for the vapor. This scheme satisfies $N = N_l + N_v$ and $V = V_l + V_v$ by construction. The estimated liquid and vapor densities are then:

$$\rho_{l,v} = \frac{N_{l,v} m}{V_{l,v}}, \tag{4.5}$$

where m is the atomic mass of Pt, $m = 195.1$ amu.

4.4 Results

4.4.1 "French Fry" Geometry

The left image in Figure 4.2 depicts the slab-like geometry of one of the 256 atom liquid-vapor systems, where the majority of the particles exist within a homogeneous liquid, on the inside of the density cut-off isosurface at $\tilde{n}_{avg}$. The DFTMD simulations were initialized with an equilibrated cell of liquid with two cells of the same size at vacuum added to

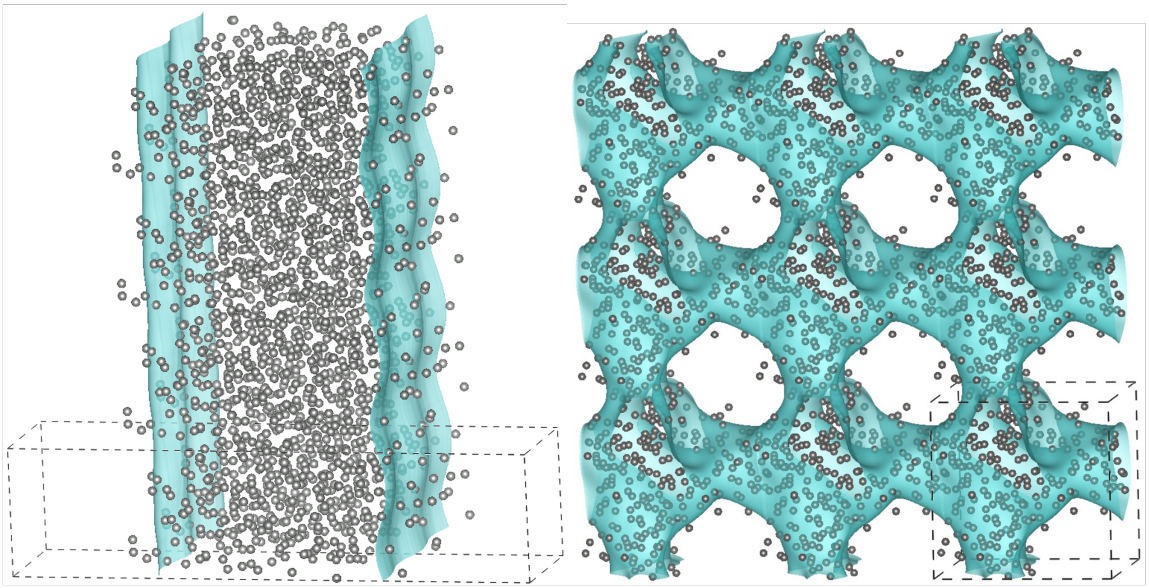

Figure 4.2: Snapshots from the simulations of the 256-atom french fry (left) and Swiss cheese (right) systems at 6000 K and 5.00 g/cm^3. Atoms within the instantaneous interface (isosurface) are in the liquid phase and those outside of the isosurface are in the vapor phase. The unit cell is marked by dashed lines and has been replicated in order to better illustrate the topology of the liquid-vapor interface.

either side in the x-direction. The system was then slowly compressed and deformed until an aspect ratio of 4:1 in the x-direction was achieved. The simulation was then run for several temperatures along the 5.00 g/cm^3 isochore. As the simulations progressed in time, we saw the liquid either compress or expand depending on temperature, while particles near the liquid interface vaporized, expelling particles into the vacuum. The simulation cell in Figure 4.2 has been replicated in space to enhance visualization. The phase boundary estimates for this system are shown in Figure 4.3, represented by the green points.

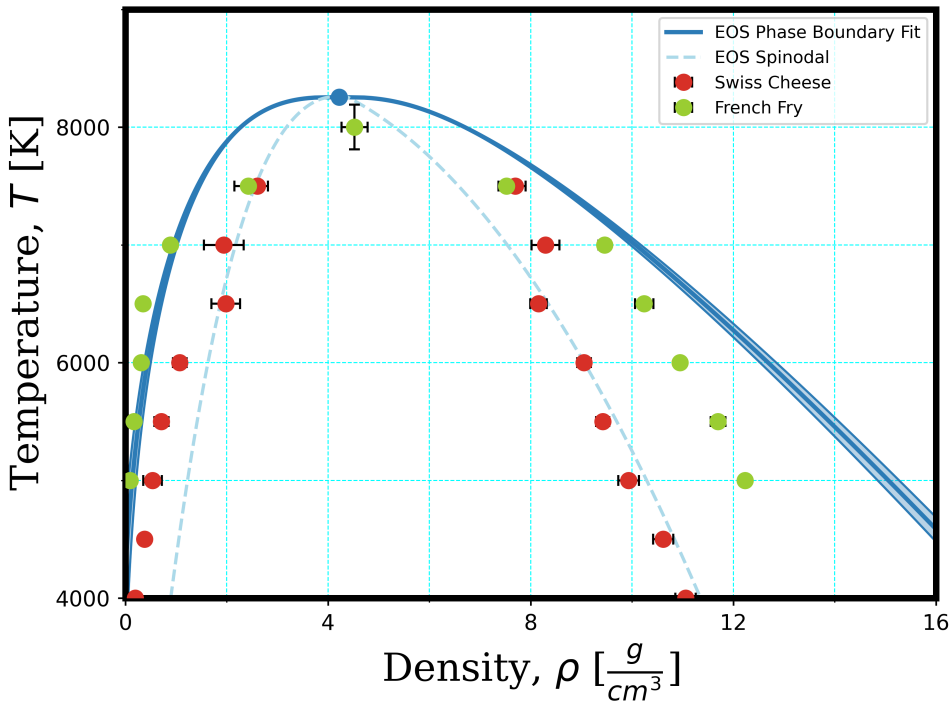

Figure 4.3: Comparison of the platinum liquid-vapor phase boundary calculated from the instantaneous interface calculations (red and green points) and the EOS fit [9] (blue), including both the spinodal and binodal curves, for the 256-atom system.

4.4.2 "Swiss Cheese" Geometry

The right image in Figure 4.2 shows the positions of the atoms for one snapshot of the 256 atom Swiss cheese DFTMD simulation. These simulations were initialized with a cubic cell homogeneously filled with fcc platinum and ran for approximately 10000 1-fs time steps until it was equilibrated with respect to the pressure. The interface represents the isosurface located at $\tilde{n}_{avg}$. Again, the simulation cell has been replicated to better illustrate the partitioning of the system. This snapshot shows a fully connected liquid network containing a large "bubble" inside of which is vapor. Over time, we see the systems that

are inside of the coexistence region tend to cycle through different compositions: changing from mostly liquid with bubbles to mostly vapor with droplets, as well as various sheet-like configurations. The phase boundary estimates for this system are shown in Figure 4.3, represented by the red points.

4.4.3 Spinodal to Binodal Mapping

In the thermodynamic limit the spinodal points mark the transition from unstable to metastable states. However we found that the bounds on the coexistence curve obtained from the instantaneous interface calculations for the Swiss cheese system span the space between the local pressure extrema, P_{lmin} and P_{lmax} (blue lines in Figure 4.4), as opposed to V_{liquid} and V_{vapor} (red lines in Figure 4.4). We found overall that these estimates align well with the spinodal obtained from the EOS calculation in the previous chapter [9]. This is shown in Figure 4.3 when compared to the EOS spinodal curve.

We corrected the estimated liquid-vapor phase boundary obtained from the instantaneous interface calculations under the assumption that they correspond to the spinodal. With this correspondence in mind, we established a scaling relationship between the EOS binodal and EOS spinodal points, then re-mapped the estimated Swiss cheese instantaneous interface phase boundary by applying the following empirical transformation:

$$\rho^{v}_{bin} = \rho^{v}_{spin} - \frac{1}{2}\left(k_1 x^{\beta} + k_2 x^{\beta+\Delta}\right) + k_3 x, \tag{4.6}$$

$$\rho^{l}_{bin} = \rho^{l}_{spin} + \frac{1}{2}\left(k_1 x^{\beta} + k_2 x^{\beta+\Delta}\right) + k_3 x \tag{4.7}$$

where $k_1 = 4.16 \pm 0.28$, $k_2 = 6.69 \pm 0.68$, and $k_3 = 4.57 \pm 0.11$. Here, $x = \left(1 - T/T_c\right)$ and

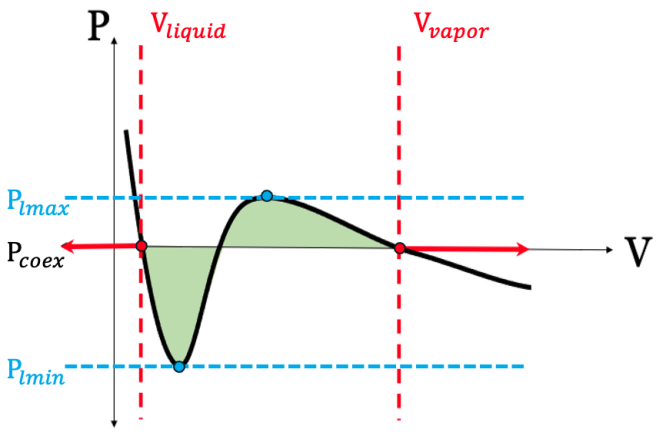

Figure 4.4: Diagram of the Maxwell equal area construction for a typical isotherm displaying a van der Waals loop. The red points indicate the binodal points where the system transitions from a state of liquid-vapor coexistence to a homogeneous liquid (left) and vapor (right). The blue points are the spinodal points. The regions of the isotherm between the red lines and blue points are metastable states, while the region between the two blue points, where the pressure increases with increasing volume, are unstable.

the exponential constants, β and Δ, are those used for the Wegner fit of the liquid-vapor phase boundary, $\Delta = 0.5$ and $\beta = 0.325$. For $x = 0$, we enforce $\rho_{bin} = \rho_{spin}$ for both the liquid and vapor expressions. These re-mapped points are then fit to the Wegner equations (4.8, 4.9) [60] to produce a phase boundary curve.

$$\rho_v = \rho_c - \frac{1}{2}\left(C_1 x^{\beta} + C_2 x^{\beta+\Delta}\right) + C_3 x \tag{4.8}$$

$$\rho_l = \rho_c + \frac{1}{2}\left(C_1 x^{\beta} + C_2 x^{\beta+\Delta}\right) + C_3 x \tag{4.9}$$

We found that the resulting re-mapped liquid-vapor phase boundary agrees well with the EOS phase boundary and the re-mapping produces a critical point that agrees well with those calculated from the EOS [9].

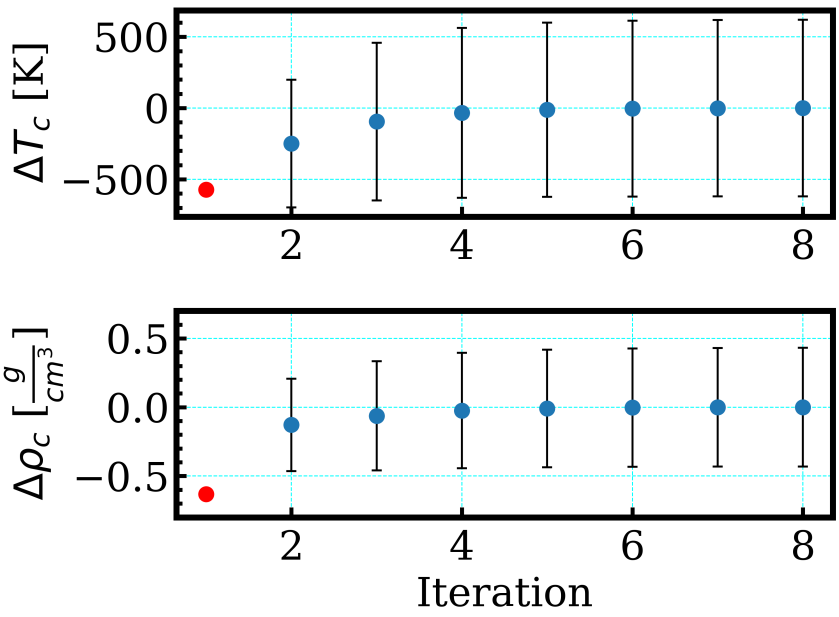

Figure 4.5: Iteratively solved critical point for the instantaneous interface calculation from a fit to the mapped binodal points of the 256-atom system.

Based on this, we applied a mapping equation of a similar form to perform the transformation from the spinodal curve to the binodal curve, again using the same values for the critical exponents (4.6) and (4.7). Defining the mapping in terms of

$$x = \left(1 - \frac{T}{T_c}\right), \tag{4.10}$$

as opposed to simply T, we ensured by construction that at $T = T_c$ the value of the binodal and spinodal are equal. However, in doing so we also introduced a dependence on the critical temperature. For the instantaneous interface calculation T_c is unknown initially so we first applied the mapping to the instantaneous interface raw data using the T_c found from the EOS fit [9] for the corresponding system size (red point in Figure 4.5). We

then found the critical point of the instantaneous interface calculation using the Wegner equations. For a self-consistent mapping of the instantaneous interface raw data to its binodal-like curve, we found the critical point iteratively, substituting T_c in equation (4.10) with the critical temperature found using the Wegner equations. The evolution of the critical temperature over the iteration is shown in Figure 4.5.

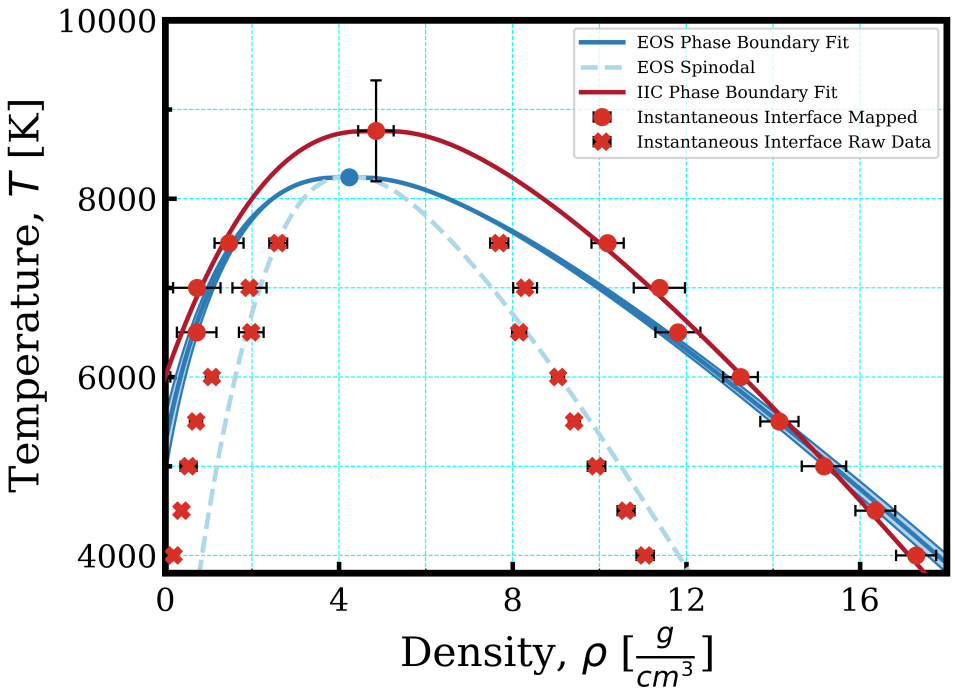

Figure 4.6: Comparison of the raw (xs) instantaneous interface calculation results and the mapped (circles) values for the Swiss cheese system (red) with the results from the EOS analysis (blue) [9].

In order to define the mapping coefficients we look at the difference in the EOS binodal and spinodal curves:

$$\rho_{bin}^{EOS} = \rho_c \pm \frac{1}{2}\left(C_1 x^{\beta} + C_2 x^{\beta+\Delta}\right) + C_3 x \tag{4.11}$$

$$\rho_{spin}^{EOS} = \rho_c \pm \frac{1}{2}\left(C_4 x^{\beta} + C_5 x^{\beta+\Delta}\right) + C_6 x \tag{4.12}$$

$$\rho_{bin}^{mapped} = \rho_{spin}^{IIC} \pm \frac{1}{2}\left((C_1 - C_4) x^{\beta} + (C_2 - C_5) x^{\beta+\Delta}\right) + (C_3 - C_6) x, \tag{4.13}$$

where $C_1 = 9.6 \pm 0.2$, $C_2 = 18 \pm 0.4$, $C_3 = 8.6 \pm 0.1$, $C_4 = 5.5 \pm 0.1$, $C_5 = 11.4 \pm 0.2$, and $C_6 = 4.1 \pm 0.1$.

4.4.4 Phase-Boundary Sensitivity

There exist multiple methods of calculating the instantaneous interface calculation coarse-graining length, ξ, and the interface density cut-off, ρ_{cut} [65, 53]. To test the sensitivity of the critical point calculation to the choice of parameter, we have varied the ξ and ρ_{cut} values by up to 50% and recalculated the critical point for these new values. The results of this investigation are shown in Figure 4.7. We found that the instantaneous interface calculation is robust across the span of different ξ values for both geometries: at most producing a difference in critical temperature of approximately 10% and a difference in critical density of approximately 5%. On average, we saw a change in critical point quantities of approximately 4%. The dependence of the critical point on the value of ρ_{cut} is notably stronger, particularly with the Swiss cheese system. For the Swiss cheese simulation, the differences in the critical temperature are as large as 37% and differences in the critical density reach approximately 92%. While the sensitivity to the density cut-off is less pronounced for the french fry calculation, it is still notably stronger than the depen-

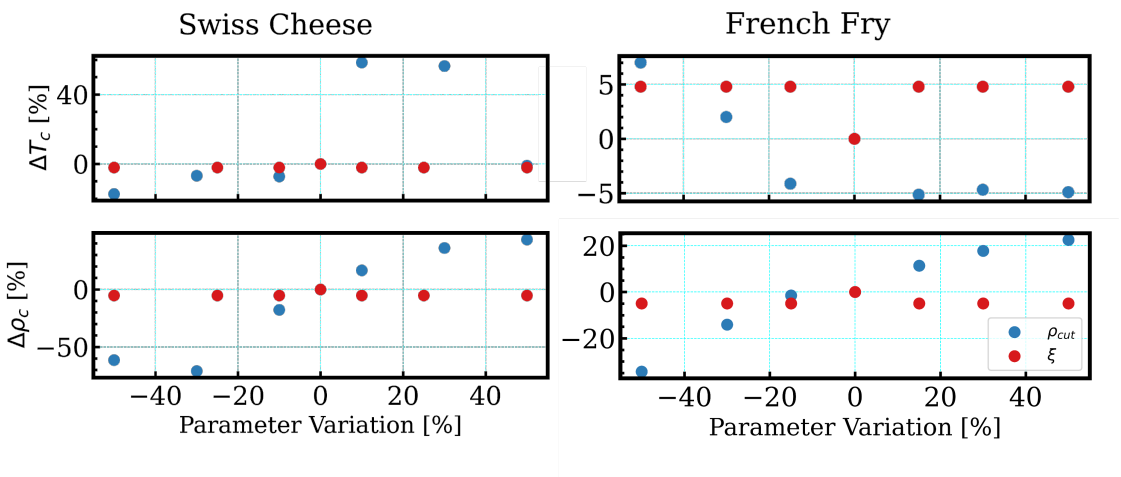

Figure 4.7: Comparison of critical point parameters for a range of different coarse-graining lengths and density cut off values. Results for the Swiss cheese are on the left, while those for the french fry are on the right. The y-axis represents the percent difference in the calculated critical points extrapolated from the results shown previously in Figure 4.3.

dence on the coarse-graining length for the same system. The change in the critical density for the french fry system is as high as almost 30%.

For the Swiss cheese simulations, we investigated the results of the instantaneous interface calculation for the different sized systems, as we did in our previous study [9]. We find that this calculation is much more sensitive to finite size effects than the EOS fitting method. There is substantial variation in the slopes on either side of the phase boundary for the different sized systems. We hypothesize that the difference in the sensitivities of the liquid-vapor phase boundary are a consequence of the relatively poor representation of the vapor phase within the instantaneous interface calculation. This is also illustrated in Figure 4.6, where the majority of the vapor-side of the phase boundary exists at negative densities for the remapped data—an entirely unphysical result. It is worth noting that the

estimated number of atoms in the vapor phase is typically very small. For example we found that the vapor phase was composed of fewer than 10 atoms on average in the 256 atom cell at the lowest temperature sampled. We were unable to perform the instantaneous interface calculation for simulations above 7000 K for the 32-atom system due to the absence of any atoms inside the vapor region.

4.5 Discussion

In summary, we have implemented the instantaneous interface calculation method [65] for studying an atomic system within the liquid-vapor coexistence region. We have performed an investigation of the impact that the geometry of a system can have on the estimate of the liquid-vapor phase boundary and critical point. It has been previously posited that this technique is robust to "reasonably arbitrary geometries," however our results have shown that, at least for some cases, the dependence on the geometry is non-negligible. A previous study [69] looked at the affects of implementing a mean-field based MD simulation to represent fluids and found that the offset of the extremum of the resulting vdW-like loops from the "true" phase boundary is proportional to the interfacial surface to volume ratio. To explore this idea we have calculated the average surface area of the liquid-vapor interface for the different geometries, shown in Figure 4.8. Across the range of temperatures the interfacial surface area for the Swiss cheese geometry is higher than that of the french fry. The overall average surface area for the Swiss cheese system is 1330 ± 155 Å^2 and for the french fry is 527 ± 37 Å^2. This supports the idea that the degree of metastability of the coexisting phases is partially dependent on the surface area of the interface. For the french fry geometry we found a phase boundary that is closer to the binodal of the Pt EOS caluclated in our previous publication [9], while the Swiss cheese is much closer to the

spinodal of the EOS. In addition to the difference in the average interfacial surface area, the Swiss cheese system also has much larger error bars than the french fry system. This is due to the variation of the atom configurations over time as the system fluctuates through the bubbles and droplets.

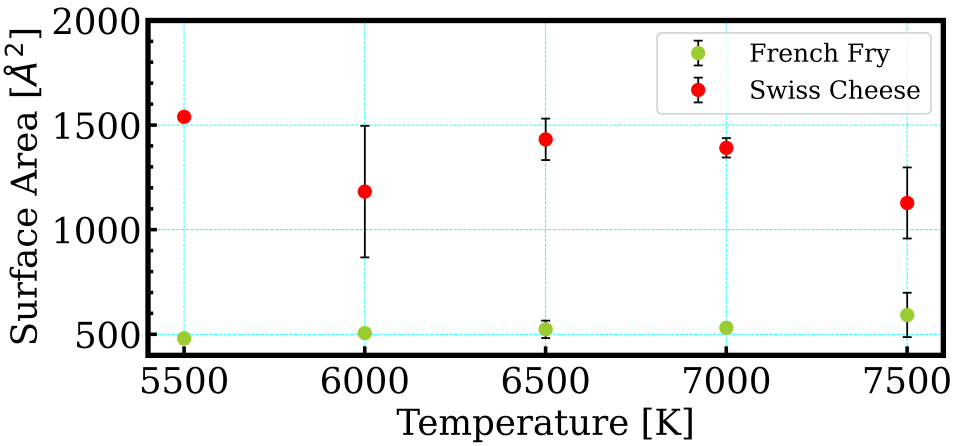

Figure 4.8: Comparison of the average interfacial surface area for the french fry system (green) and the Swiss cheese system (red) for the range of temperatures simulated.

A previous implementation of the instantaneous interface calculation [53] conducted an analysis of the liquid and vapor densities by collapsing the 3-dimensional system into a 1-dimensional problem. A 1-dimensional profile of the density is fit to determine the liquid and vapor densities, averaged over time, as well as the width of the interface. This approach is not applicable to the Swiss cheese geometry because of the complete asymmetry present in every direction, which cannot be realized within a 1-dimensional density profile. For the french fry geometry, this approach cannot resolve any curvature in the interface surface and the presence of such curvature results in a smeared out interface making the location of the interface less certain. Additionally, the liquid density that is extracted from the fit corresponds to the middle of the liquid slab, as opposed to our approach where

we have considered the average of the entire liquid region. By sampling the density such that it is weighted toward the more dense middle of the french fry, the liquid-vapor phase boundary is skewed towards a higher density liquid. We have attempted to assuage these biases by performing a 3-dimensional analysis of the coarse-grained density field, which allowed us to preserve any complex geometries.

As stated previously, this is a follow up to the previous chapter [9] in which we calculated the liquid-vapor critical point and phase boundary of platinum via a Maxwell construction applied to an equation of state fit of our DFTMD data, which is shown in Figure 4.3. In that study we also performed a sensitivity review for our calculations based on various aspects of the analysis. We have found that in general the method of characterizing the critical behavior from fitting an EOS to the DFTMD is less sensitive to the details of the calculation than the instantaneous interface calculations. However, the approach of the instantaneous interface calculation is significantly less computationally expensive than the EOS fit. To adequately represent the system such that it can be fit to an EOS we needed to perform many calculations for a range of temperatures and densities in order to produce a series of isotherms, including temperatures outside of coexistence. However, for the instantaneous interface calculation we needed a range of temperatures encompassing the coexistence region for a single isochore. This is highly advantageous when dealing with limited computational resources.

4.6 Conflict of Interest

The authors have no conflicts to disclose.

4.7 Data Availability

The data that support the findings of this study are available from the corresponding author upon reasonable request.

4.8 Acknowledgements

Sandia National Laboratories is a multi-mission laboratory managed and operated by National Technology & Engineering Solutions of Sandia, LLC, a wholly owned subsidiary of Honeywell International Inc., for the U.S. Department of Energy's National Nuclear Security Administration under contract DE-NA0003525. This paper describes objective technical results and analysis. Any subjective views or opinions that might be expressed in the paper do not necessarily represent the views of the U.S. Department of Energy or the United States Government.

Chapter 5

DC Electrical Conductivity of Platinum From *Ab-initio* Simulations

The contents of this chapter were originally published as part of *Meghan K. Lentz, Joshua P. Townsend, Kyle R. Cochrane; DC electrical conductivity of platinum from ab initio simulations. AIP Conf. Proc. 26 September 2023; 2844 (1): 320003.* Minor edits within this dissertation have been made to clarify the text.

5.1 Abstract

Platinum is a highly unreactive transition metal whose properties make it desirable for experiments at Sandia National Laboratories' Z Pulsed Power Facility (Z). In order to improve the use of platinum as a material standard in shock compression experiments, we investigated the necessary procedure to produce high quality DC electrical conductivity

calculations from density functional theory using the Kubo-Greenwood (KG) approximation. We studied the effects of changing several parameters involved in these calculations, all of which have some level of control over the calculated electrical conductivity. These parameters include the sampling of the Brillouin zone, smearing of the KG energy differences, the number of virtual orbitals included in the calculations, and the number of atomic configurations that are considered in the average electrical conductivity.

5.2 Introduction

Platinum is an unreactive metal with a high melting point whose face-centered cubic crystal does not display any experimentally observed phase changes up to melt. Due to these properties, platinum is frequently used as a material standard, particularly in high-pressure and shock compression physics [48]. For the experiments conducted at Sandia National Laboratories' (Sandia) Z Pulsed Power Facility (Z), it is important to understand material properties for a large portion of phase space. Experiments on Z are subjected to very large currents and magnetic fields, thus, understanding the electrical conductivity of materials being used as standards is important [71]. Current experimental diagnostics are often unable to diagnose the thermodynamic regimes relevant to Z, leading to a reliance on *ab initio* theory. In this study, we report the results of a systematic investigation of the DC electrical conductivity of platinum using density functional theory (DFT) and the Kubo-Greenwood (KG) approximation at ambient conditions, which can be compared to experimental data. The quality of the estimate is sensitive to the approximations made both in the electronic structure and the numerical evaluation of the KG formula [72]. We show that with careful calibration in a modest supercell, one can obtain a well-converged estimate of the DC conductivity.

5.3 Methods

In order to calculate the KG electrical conductivity, we first performed density functional theory based molecular dynamics (DFTMD) calculations. With the data from the DFTMD simulations we calculated the low frequency electrical conductivity of platinum. We extrapolated the calculated conductivity to zero energy to obtain the DC conductivity. Electron-phonon coupling is accounted for by averaging the electrical conductivity over several atomic configurations.

5.3.1 Molecular Dynamic Simulations

The DFTMD calculations were conducted at 300 K and ambient density, $\rho = 21.45 \frac{g}{cm^3}$. Calculations were done using VASP 5.3.3, an implementation of Kohn-Sham DFT using periodic boundary conditions and a plane-wave basis [30, 31, 32, 33]. Because we are interested in the ambient crystal, a $10e^-$ pseudopotential was used that has a $5d^9 6s^1$ valence configuration [73]. All simulations were conducted for a 108 atom cubic supercell within the NVT ensemble with a velocity scaling thermostat. The energy plane wave cutoff was set to 700 eV. The Brillouin zone was sampled at the Γ point. The exchange-correlation functional used is the Perdew-Burke-Ernzerhof (PBE) generalized gradient approximation [36]. The simulation was run for approximately 15,000 $1fs$ timesteps, and the energy and pressure were verified to be well-converged.

5.3.2 Electrical Conductivity Calculations

The essence of the KG formalism focuses on the physical interpretation of the single-particle orbitals obtained from a Kohn-Sham DFT calculation. A commonly used approximate form for the KG electrical conductivity, $\sigma_{\mathbf{k}}$, at frequency ω for a specific $\mathbf{k}$ point is given by:

$$\sigma_{\mathbf{k}}(\omega) = \frac{2\pi e^2\hbar^2}{3m^2\omega\Omega}\sum_{j=1}^{N}\sum_{i=1}^{N}\sum_{\alpha=1}^{3}[F(\varepsilon_{i,\mathbf{k}}) - F(\varepsilon_{j,\mathbf{k}})]\,|\,\langle\Psi_{j,\mathbf{k}}|\nabla_\alpha|\Psi_{i,\mathbf{k}}\rangle\,|^2\delta(\varepsilon_{j,\mathbf{k}} - \varepsilon_{i,\mathbf{k}} - \hbar\omega), \tag{5.1}$$

where e is the charge of an electron, m the electron mass, Ω the cubic supercell volume element, and $F(\varepsilon)$ the occupation from the Fermi-Dirac distribution [74, 75]. The i and j summations are over the N discrete bands included in the calculations and the α summation over the three spatial directions, respectively.

To calculate the electrical conductivity, we consider several atomic configurations from the DFTMD simulation. These atomic configurations must be statistically independent and are chosen based on an estimated correlation time, 128 fs, calculated from a block averaging of the energy. The conductivities for each snapshot are then averaged for the final electrical conductivity. The low energy spectrum of the conductivity is especially sensitive to the details of the calculation. States near the Fermi surface dominate the contribution to the conductivity in this region, but there are also significant finite size errors. Therefore, it is important when carrying out KG calculations to demonstrate convergence of the estimated conductivity with respect to both $\mathbf{k}$ point sampling as well as other effects such as smearing.

The converged estimate of the low frequency portion of the electrical conductivity with

respect to the investigated parameters is shown in Figure 5.1. Due to the finite size of the system, the lowest energy spectrum is heavily influenced by finite size errors, evidenced by a drastic drop in the conductivity below approximately 0.01 eV. In order to capture the DC conductivity, we need to extrapolate the well resolved electrical conductivity to zero energy. Looking at 5.1, showing the conductivity of the low energy region, the conductivity appears Drude-like. Therefore, we fit the KG results to the Drude model (Equation 5.2). It is important to exclude from the fit both the extremely low energy conductivities that are smaller than the typical eigenvalue separation, as well as the higher energy conductivities that have departed from the fit to the Drude model.

$$\sigma = \frac{\sigma_0}{1+\omega^2\tau^2} + constant. \tag{5.2}$$

A constant has been added to the form of the Drude model to ensure an optimal fit. From this fit, the DC conductivity can be reliably extrapolated.

5.4 Convergence Studies

Accurately evaluating the KG electrical conductivity depends on several controllable parameters. We have studied these parameters to understand how best to represent the system. Included in these convergence studies are the **k** point mesh used to sample the Brillouin zone, the smearing term which smooths out local oscillations, the virtual orbitals included in the conductivity calculation, and the number of atomic configurations the electrical conductivity is averaged over.

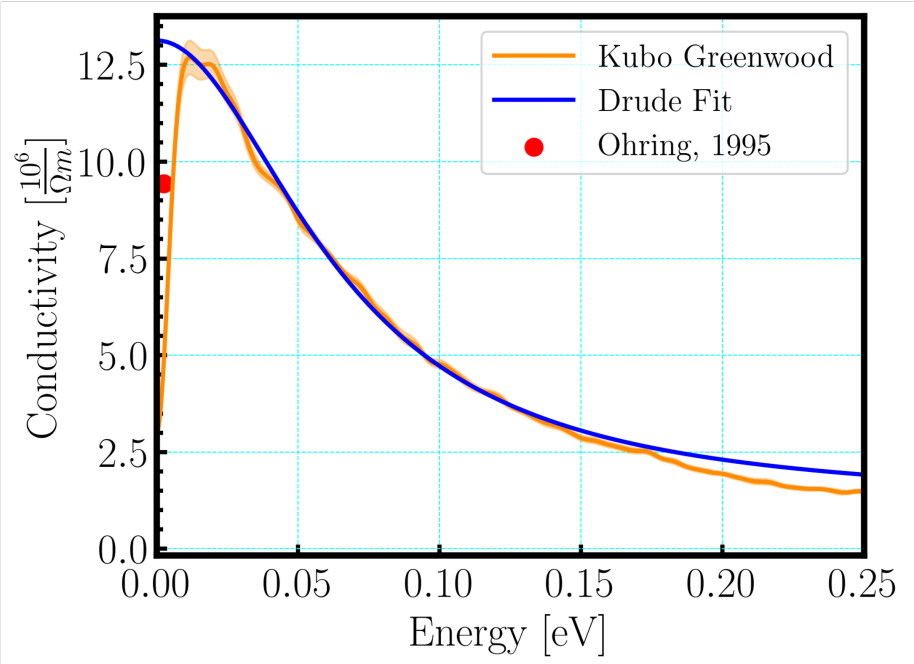

Figure 5.1: Calculated Kubo Greenwood electrical conductivity for platinum at ambient conditions shown in orange with statistical error. The conductivity fit to the Drude model is shown in blue. The measured DC conductivity, $\sigma_{DC} = 9.43\frac{10^6}{\Omega m}$, is in red [10]. Sampled over a 10x10x10 irreducible wedge mesh with gaussian width (Eq.) $\Delta = 0.004$ eV. Calculated using 10 snapshots and 800 total bands.

5.4.1 Brillouin Zone Sampling

The convergence of the Brillouin zone sampling is an essential step in the calculation of the electrical conductivity due to the extreme sensitivity of the DC conductivity to the **k** point mesh used. The number and location of the **k** points used determines where on the Fermi surface contributes to the conductivity calculation. For simple crystalline systems, such as copper and aluminum, which have nearly spherical Fermi surfaces, few **k** points are needed to sample the Fermi surface in order to sufficiently calculate the conductivity

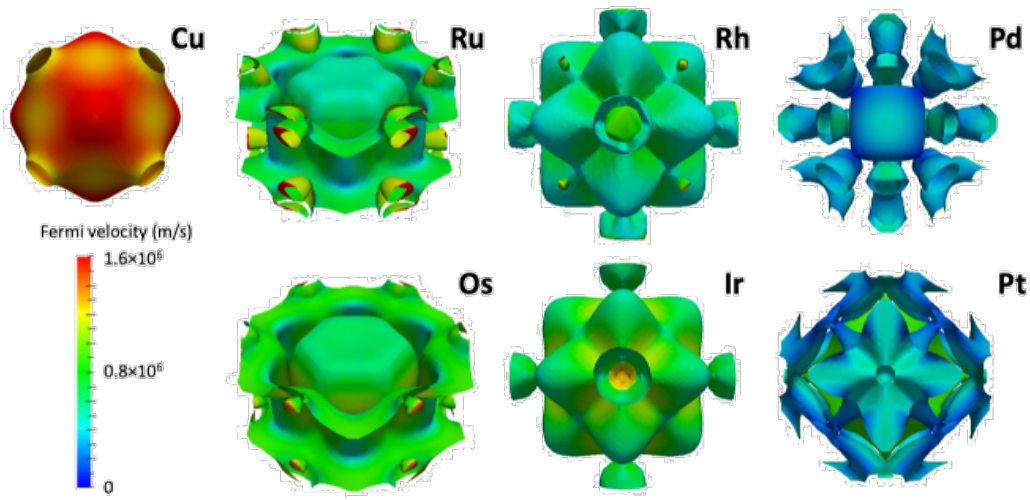

Figure 5.2: Comparison of the Fermi surfaces for Pt-group metals. Note the dramatic difference in the complexity of the Fermi surface of platinum compared to that of copper. Image taken from Dutta, et al. (2017) [11].

[75]. However, as seen in Figure 5.2 from Dutta, et al. (2017) [11], the Fermi surface of platinum is much more complex and, therefore, requires the use of more **k** points.

For this study, we have sampled the 108 atom platinum system with meshes ranging from 1x1x1 to 10x10x10. The number of **k** points increase as M^3 for an MxMxM mesh causing the higher order meshes to become too computationally expensive, thus, we used the irreducible wedge for the samplings larger than a single **k** point. To do this, we give VASP an explicit set of **k** points for which we ignore the breaking of symmetries caused by thermal fluctuations and assume the full set of symmetries are present. We have considered both Γ-centered grids and the shifted Monkhorst-Pack scheme. In Figure 5.3, the electrical conductivities calculated using KG are shown for the different Brillouin zone samplings (left panel), as well as the extrapolated DC conductivities from the fit to the

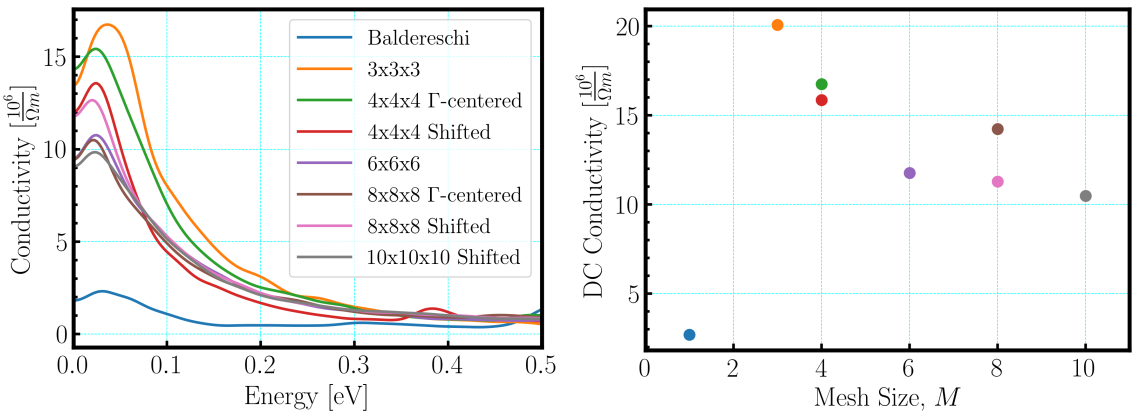

Figure 5.3: Conductivity calculated for a range of **k** point grids (left panel). Calculated using a single snapshot with 800 total bands and $\Delta = 0.02$ eV. Corresponding DC conductivities extrapolated from Drude model fit (right panel).

Drude model (right panel). For the sake of computation time, all conductivities are calculated using a single snapshot. To avoid bias, the same snapshot is used for each calculation. These results are looking only at the convergence of the DC conductivity with respect to the number of **k** points needed. From Figure 5.3, we see that the estimated electrical conductivity does not vary monotonically with respect to the number of **k** points. It is clear that a large number of **k** points are necessary to calculate a converged DC conductivity and that the spread in calculated conductivities is very large for the different **k** point meshes [72].

5.4.2 Discrete Band Structure Smearing

Another variable that has a large influence over the calculated electrical conductivity is the smearing of the discrete KG energies. Due to the discrete energy spectrum, the δ function

in Equation 6.1 needs to be modified. In VASP 5.3.3, this is done using a Gaussian function [74]. It is important to note that different codes and different versions of the same code use different broadening functions and therefore is not necessarily transferrable.

$$\delta(\varepsilon_{j,\mathbf{k}} - \varepsilon_{i,\mathbf{k}} - \hbar\omega) \rightarrow e^{-\frac{(\varepsilon_{j,\mathbf{k}} - \varepsilon_{i,\mathbf{k}} - \hbar\omega)^2}{2\Delta^2}}, \tag{5.3}$$

where Δ is the width of the Gaussian. Previous literature [75] has suggested taking Δ equal to the average difference in energy eigenvalues immediately above and below the Fermi energy, weighted by the slope of the Fermi distribution as a starting point for finding the ideal smearing. It is suggested when choosing the amount of smearing to approach the eigenvalue spacing from below to prevent over smearing. For platinum, we have found the average difference between eigenvalues at the Fermi energy to be approximately 0.02 eV. In Figure 5.4, we have calculated the KG electrical conductivity of a single snapshot for a range of Δ.

Looking at Figure 5.4, large oscillations in the conductivity are the result of under smearing, and make robust estimation of the DC conductivity a challenge. As the smearing term increases, the KG conductivity in the figure becomes very smooth before flattening and losing its structure, which causes a notable drop in the extrapolated DC conductivity. Because it is necessary to avoid over smearing the conductivity, we preserve some minimal oscillations in the KG calculation. From this, we have determined the optimal width of the Gaussian to be between 0.003 eV, which maintains a larger degree of oscillations than necessary, and 0.005 eV, where the curve has been significantly smoothed and may be experiencing some structure loss.

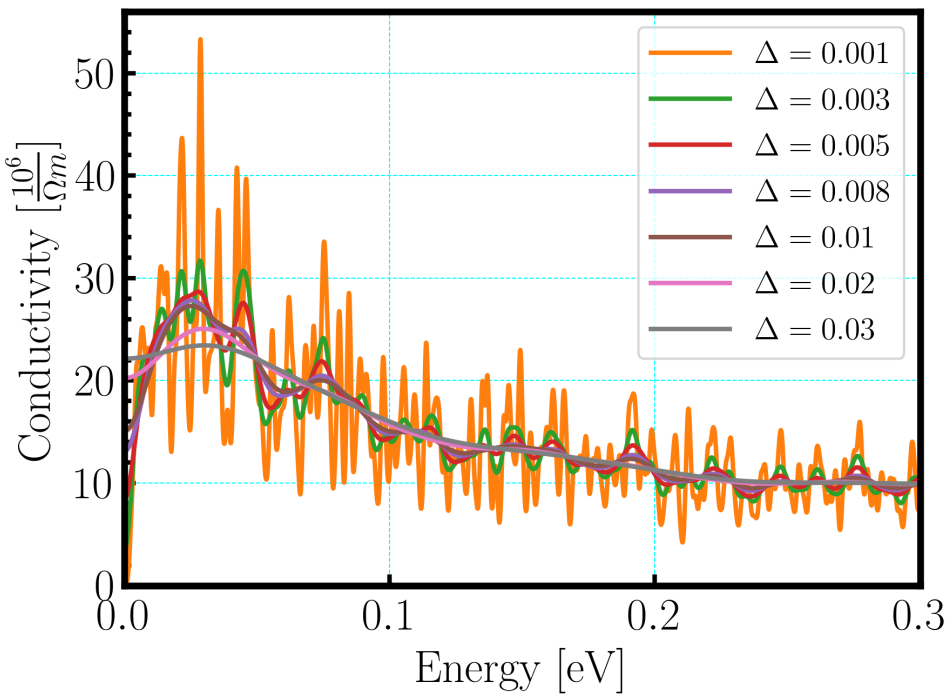

Figure 5.4: Kubo Greenwood conductivity calculations with different levels of discrete band structure smearing. Calculations were sampled with a 4x4x4 shifted grid for expediency, using the irreducible wedge. Calculated from a single snapshot and 800 bands.

5.4.3 Number of Orbitals

In principle, the conductivity can be calculated to arbitrarily high frequencies by including sufficiently many virtual orbitals. In practice, only finitely many virtual orbitals can be considered. A common way to check the convergence of the calculated electrical conductivity is through the evaluation of the well-known sum rule (Equation 5.4) [75, 74]. It becomes clear in Figure 5.5 that the inclusion of a very large number of orbitals is necessary for the total KG electrical conductivity to converge. However, the additional higher energy bands are unoccupied and contribute very little to the low frequency conductivity.

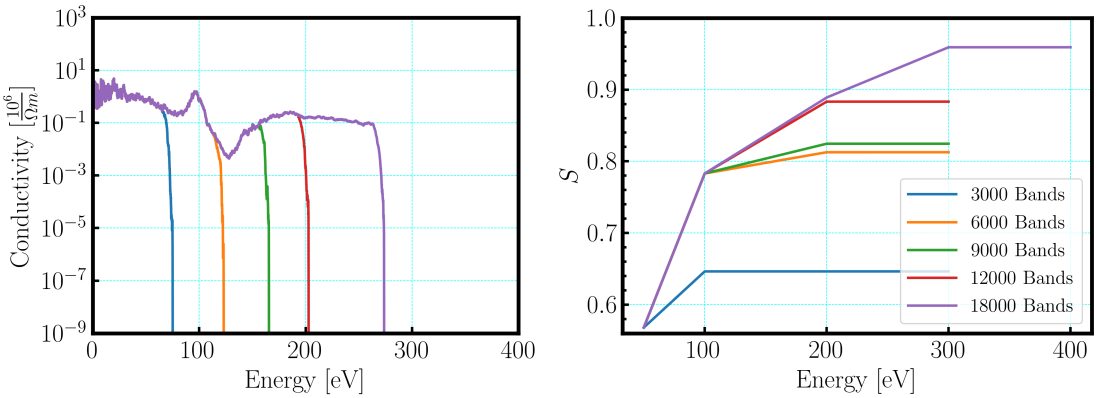

Figure 5.5: Electrical conductivity for several systems of different sizes (left). f-sum rule calculations increasing the maximum energy difference required for excitation pairs to be included in conductivity calculations (right). The discrete system size prevents the high frequency conductivity from being resolved due to the lack of sufficient orbitals included in the calculation, indicated by the sudden drop in the conductivity. The DC conductivity remains the same as the size of the system decreases to 800 bands.

$$S = \frac{2m\Omega}{\pi e^2 N_e} \int_0^\infty \sigma(\omega) d\omega = 1 \tag{5.4}$$

In addition to our sum rule calculations, we also extrapolated the DC conductivities for systems of varying sizes, finding that the DC conductivity does not change for the range of 800 to 2000 bands. For the purposes of this work, we are interested in finding the DC conductivity of our system, looking only at the low energy conductivity, between 0.0-0.5 eV. Due to this, we require fewer virtual orbitals without the convergence of the sum rule. We have included approximately 800 total bands, greatly decreasing computation times.

5.4.4 Number of Snapshots

Lastly, we ran calculations looking at the necessary number of atomic configurations to be included in the conductivity calculation. By averaging the conductivity calculation over a number of different atomic configurations, we are able to capture the effects of electron-phonon coupling. Snapshots were taken from the end of the DFTMD ambient calculation to ensure equilibration. The KG electrical conductivity was then calculated including 1, 5, 10, 15, and 19 snapshots. From Figure 6.1, it is clear that considering only a single atomic configuration is not representative of the converged KG conductivity; however, a rather small number of configurations (10) is sufficient to see the system converge with relatively small error.

5.5 Remarks and Future Work

In Figure 5.1, we have combined all of the findings from the convergence studies in order to determine the DC conductivity for platinum at ambient conditions. For this calculation, the number of energy points where the conductivity is calculated is 40,000 and the number of bands 800, corresponding to approximately 250 virtual orbitals. The Brillouin zone is sampled using the shifted 10x10x10 irreducible wedge, Δ is set to 0.004 eV, and we have averaged over 10 snapshots. This work has not yet accounted for the finite simulation size. The calculated Drude DC conductivity for this calculation is $13.1 \pm 0.7 \frac{10^6}{\Omega m}$, which is within 28% of the measured value $9.43 \frac{10^6}{\Omega m}$. This level of error is not uncommon for calculations of the DC electrical conductivity using the KG approximation. Previous literature reports errors of up to 30% [75] and up to 50% [72].

This method of calculating the electrical conductivity has shown great success in study-

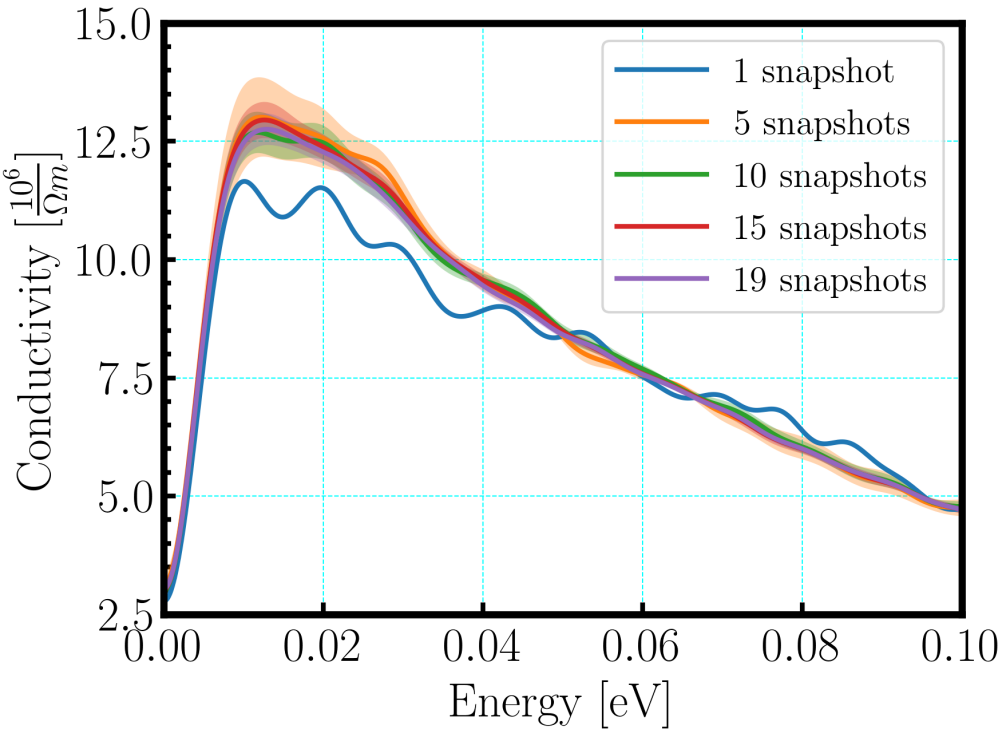

Figure 5.6: Kubo-Greenwood conductivities calculated with contributions from a varying number of atomic configurations, including statistical error. Calculated including 800 bands sampled with a 10x10x10 shifted mesh and $\Delta = 0.004$ eV.

ing many different systems, particularly those in the hot dense regime [72, 76], however, it does have its limitations. Although DFT is in principle an exact theory, the exact functional is unknown. Therefore, approximate forms are used, which introduce systematic inaccuracies that are difficult to quantify.

In summary, we have shown that the successful calculation of the DC electrical conductivity using the KG approximation requires a level of fine tuning. The calculated electrical conductivity is highly dependent on the sampling of the Brillouin zone, especially for materials like platinum with a complex Fermi surface. Applying sufficient smearing to the

KG electrical conductivity is also vital in reducing the amount of noise in the low energy region. Conversely, applying too much smearing results in the flattening of the conductivity curve, causing the calculated DC electrical conductivity to decrease substantially. We have also shown that convergence of the full optical conductivity is not necessary when interested in only the low energy electrical conductivity. Capturing the electron-phonon coupling does require the calculation of more than one atomic configuration; however, a relatively small number of configurations is suitable for calculating the KG electrical conductivity for this material at this density and temperature.

5.6 Acknowledgements

We would like to thank Mike Desjarlais for many helpful discussions. Sandia National Laboratories is a multimission laboratory managed and operated by National Technology & Engineering Solutions of Sandia, LLC, a wholly owned subsidiary of Honeywell International Inc., for the U.S. Department of Energy's National Nuclear Security Administration under contract DE-NA0003525. This paper describes objective technical results and analysis. Any subjective views or opinions that might be expressed in the paper do not necessarily represent the views of the U.S. Department of Energy or the United States Government.

Chapter 6

Electrical Conductivity of Platinum French Fries and Swiss Cheese

6.1 Abstract

Due to the high pressures and temperatures typically involved at the liquid-vapor critical point of metals, experimental data in this regime is rare. Measurements of the electrical conductivity in the liquid-vapor coexistence region are not possible to capture for all but the lowest melting point metals. Due to these difficulties, there is a heavy reliance on theoretical calculations to characterize transport properties near the critical point. We have performed density functional theory molecular dynamics simulations in the region of phase space around the liquid-vapor coexistence region for platinum in order to study the electrical conductivity. Conductivities are calculated using the Kubo-Greenwood approximation. In addition to a range of temperatures and densities studied, we also compare the electrical conductivity for two different geometric configurations of the two-phase system

to quantify anisotropic effects.

6.2 Introduction

Understanding the electronic properties of metals within the region of liquid-vapor coexistence is a difficult, but important scientific endeavor. The continued development of technology is heavily reliant on a deep understanding of the underlying materials being used and enables continued technological advancements in many fields. For applications in pulsed power experiments [75, 77, 78], materials are frequently subjected to very high temperatures and pressures resulting in materials entering the coexistence region during experiments. The presence of high voltages and currents amplifies the importance of understanding the transport properties of these materials under these conditions [79, 80, 81]. Accurate transport properties of these materials under high voltages and currents are also important to astrophysical research. As a planetary body cools during the formative stages, supercritical fluids play an important role which requires an understanding of material in coexistence [41].

As metals traverse different regions of phase space, there are often associated transitions in the electrical properties of the system. Data concerning these expanded metals, particularly the electrical conductivity, is typically only available for metals with low melting points such as mercury [43, 42], due to current diagnostic limitations. This has led to a reliance on theoretical techniques for characterizing materials transport properties. In addition to the lack of experimental measurements, theoretical simulation is also difficult due to the complexities of electrical conductivity within the liquid-vapor coexistence region. There have been observed metal-nonmetal (MNM) transitions within fluid metal coexis-

tence, however a continuous MNM transition is not necessarily guaranteed. Because of the presence of these MNM transitions, techniques used to study free-electron-like fluids are not applicable in much of this region of phase space [82]. Those systems that are experimentally accessible have indicated that there does not exist a universal behavior of electronic properties within coexistence [42].

We have performed density functional theory molecular dynamics (DFTMD) calculations for a range of temperatures and densities of platinum (Pt) surrounding the liquid-vapor coexistence region. To calculate the electrical conductivity we have used the Kubo-Greenwood (KG) approximation, averaging over several snapshots in time. For these electrical conductivity calculations we consider two different geometries for the Pt unit cell, a heterogeneous cube—resembling a block of Swiss cheese—and a continuous slab—resembling a french fry. We have found that the electrical conductivity depends strongly on the geometry of the system. For entirely anisotropic volumes, determining the effective DC conductivity of the macroscopic system is not a straightforward task.

6.3 Methods

DFTMD calculations were performed using the Vienna *ab initio* simulation package (VASP) [30, 31, 32, 33] with the same initial conditions as described in Chapter 2 [9] and Chapter 3 of this dissertation, where we have considered a range of temperatures, 6000-12000 K, and densities, 4.00-10.00 g/cm^3 for the homogeneous cube. Additionally, we performed DFTMD simulations along a 5.00 g/cm^3 isochore for the temperature range 5000-8000 K for both geometries. VASP implements a planewave basis and periodic boundary conditions. We have used a 10 e$^-$ platinum pseudopotential [56] and the energy planewave

cutoff was set to 700 eV. The exchange-correlation energy was computed with the Perdew-Burke-Ernzerhof (PBE) generalized gradient approximation [36] and all simulations were conducted within the NVT ensemble with a velocity scaling thermostat [57]. From our analysis of the reported DFT data [9], we have estimated a critical point for platinum of $\rho_c = 4.18 \pm 0.09$ g/cm^3, $T_c = 8120 \pm 60$ K, and $P_c = 5.56 \pm 0.50$ kbar and additionally predicted a liquid-vapor phase boundary. Here we will use the results of our MD simulations in order to calculate the electrical conductivity of platinum in this region of the phase diagram.

6.3.1 Electrical Conductivity Calculations

For our conductivity calculations we will be implementing the Kubo-Greenwood approximate formula [83, 84, 85, 74, 75]:

$$\sigma(\omega) = \frac{2\pi e^2\hbar^2}{3m^2\omega\Omega}\sum_{j=1}^{N}\sum_{i=1}^{N}\sum_{\alpha=1}^{3}[F(\varepsilon_i) - F(\varepsilon_j)]\,|\langle\Psi_j|\nabla_\alpha|\Psi_i\rangle|^2\delta(\varepsilon_j - \varepsilon_i - \hbar\omega), \qquad (6.1)$$

where e is the charge of an electron, m the electron mass, Ω the supercell volume element, and $F(\varepsilon)$ the occupation from the Fermi-Dirac distribution.

Following our previous work [58], we conducted several convergence studies to determine the parameters of our conductivity calculations. For the discrete band structure smearing term, we have used the value $\Delta = 0.003$ eV. For the sampling of the Brillouin zone, we have utilized a k-point grid that is a 4x4x4 Monkhorst-Pack irreducible wedge mesh. The results are averaged over 20 independent snapshots from the DFTMD simulations. A large enough number of orbitals were used to ensure each calculation included unoccupied energy bands in accordance with the convergence studies.

6.4 Results

Figure 6.1 illustrates the liquid-vapor phase separation for one snapshot in time from each of the different geometries where the unit cells have been periodically replicated. The simulations shown were conducted at a temperature of 6000 K and a density of 5.00 g/cm^3. The image on the left is has an exposed surface in the x and y direction, which causes a tall skinny simulation cell in the z direction, we refer to this as the "french fry" geometry. Alternatively the figure on the right demonstrates a simulation cell that is periodic in all three directions, where the phase separation leads to voids in the simulation cell, we refer to this as "Swiss cheese". To initialize the simulations for the case of the french fries, we use a near-equilibrated cell of liquid with two equally sized cells at vacuum attached to either side of the liquid in the x-direction. To initialize the Swiss cheese configurations we begin with fcc platinum homogeneously distributed in a cubic cell. All simulations were run for a sufficient number of time steps such that they are equilibrated with respect to the pressure.

6.4.1 Temperature Dependence: Swiss Cheese

The calculated Kubo-Greenwood electrical conductivity in the *x, y,* and *z* directions for three different temperatures of the Swiss cheese geometry at a single instance in time (left), as well as the corresponding atomic configurations (right) are shown in Figure 6.2. The variation in the conductivity along the individual cartesian directions illuminates the complexity of the conductivity calculations within liquid-vapor coexistence (middle, bottom) opposed to a one phase system (top). The top image is of a snapshot at 12000 K, which exists outside of the liquid-vapor coexistence region. The directional components

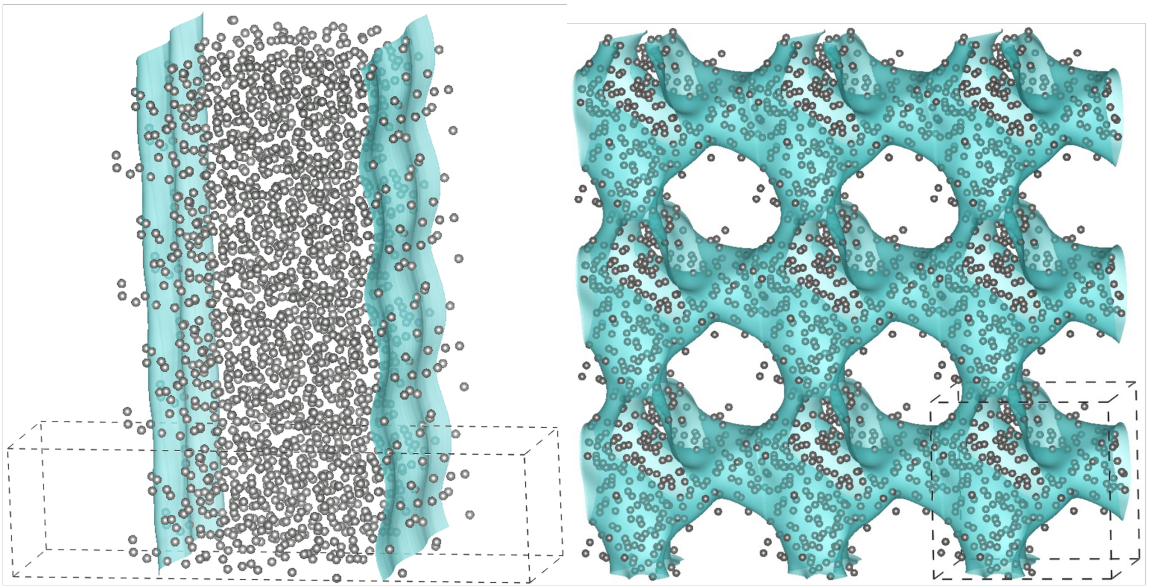

Figure 6.1: Snapshots from one of the simulations of the 256-atom french fry (left) and Swiss cheese (right) systems at 6000 K and 5.00 g/cm^3. Atoms inside the isosurface are in the liquid phase and those outside of the isosurface are in the vapor phase. The unit cell of each system is marked by dashed lines and has been replicated in order to better illustrate the phase separation.

for the electrical conductivity are the same, indicative of a homogeneous system. To calculate the effective electrical conductivity of this system, we can simply take the trace of the conductivity tensor averaged over time. The other two atomic configurations shown in Figure 6.2 are for temperatures inside the coexistence region at 7000 K (middle) and 6000 K (bottom). The atomic configurations at these two temperatures illustrate varying degrees of directional uniformity. The atomic configuration at 7000 K is not uniform in any direction, while at 6000 K a liquid phase emerges that is uniform in the y and z directions. Comparing the conductivities, the 7000 K snapshot has less spread between the different components due to the apparent lack of a bulk direction. The uniformity in the y and z direction of the 6000 K snapshot result in much larger values of the conductivity in these

directions. Although the conductivity is continuous its not entirely symmetric resulting in the y and z components being slightly different. To calculate an effective conductivity, an average over the snapshots would be used, however this proved to be less straightforward for this system. For the Swiss cheese geometry, the atomic configurations fluctuate over time resulting in major shifts in the connectivity and structure of liquid and vapor phases. These fluctuations also result in a changing electrical conductivity over time.

To understand whether the change in the conductivity across the temperature range is due to the changing ionic configuration or a dramatic change in the electronic structure we have plotted the quantity, ζ, which is akin to the mean ionization of the system. We define ζ as:

$$\zeta \equiv \frac{1}{N} \int_{\varepsilon_F}^{\infty} g(\omega) F(\omega) d\omega, \tag{6.2}$$

where N is the total number of atoms, ε_F is the Fermi energy, $g(\omega)$ is the density of states, and $F(\omega)$ is the Fermi function. In Figure 6.3, we have plotted ζ for various temperatures along an isochore for the Swiss cheese cell. We see that ζ increases linearly as a function of temperature which suggests that the system does not experience an abrupt dramatic change in the electronic structure, indicating that the change in the electrical conductivity is due to the geometry of the ions.

6.4.2 Comparing Geometries

While not an exact representation of the bulk liquid, the french fry configurations and its uniformity in two dimensions should allow us to approximate the electrical conductivity for the liquid. To get an estimate for the liquid phase in coexistence, we take an average

of the conductivity in the continuous directions. The conductivity in the perpendicular direction is a much smaller contribution and thus can be excluded from our estimates. The electrical conductivity separated into the different components for each of the different geometries is shown in Figure 6.4. The results shown are for the french fry cell (left) and Swiss cheese cell (right) at a temperature of 5000 K and a density of 5.00 g/cm^3. For both geometries, we see that two of the conductivity components are notably larger than the third. For the Swiss cheese cell the conductivity from this third direction is larger—thus has a larger effect on the effective conductivity of the system than that of the uniform french fry cell.

Because of the discrete number of orbitals in our calculations, we are unable to resolve the conductivity at the zero frequency limit, therefore to estimate the DC conductivity we take a polynomial fit of the low-frequency Kubo-Greenwood conductivity data defined by:

$$\sigma(\omega) = A + B\omega^{1/2} + C\omega^{3/2}. \tag{6.3}$$

The DC conductivity is then found by extrapolating the fit to $\omega = 0$.

Figure 6.5 is showing the average electrical conductivity of the two largest components of the Kubo-Greenwood calculation (black lines) for the same snapshots shown in Figure 6.4. The polynomial fit from equation 6.3 to these averages is shown in red with the extrapolated DC conductivity shown by the red points on the y-axis. For the same temperature and density conditions, the conductivity of the Swiss cheese configuration is lower due to the influence of the nonuniformities. For the french fry cell (left) we find a DC conductivity of $\sigma_{DC} = 2.47 \pm 0.04$ x$10^5(\Omega m)^{-1}$ and for the Swiss cheese $\sigma_{DC} = 1.12 \pm 0.02$ x$10^5(\Omega m)^{-1}$.

One possible approach to try to compensate for the changing structural orientation over time that the Swiss cheese configuration undergoes is to remove any explicit directional dependence. Instead of averaging over the cartesian components, we take the highest, lowest, and median values of the conductivity at each time step and average over those. This is shown in Figure 6.6 for the same Swiss cheese simulation as in Figures 6.4 and 6.5. By disregarding the cartesian directions, we find a new DC electrical conductivity of $\sigma_{DC} = 1.49 \pm 0.02$ x$10^5(\Omega m)^{-1}$. While this has brought σ_{DC} for the Swiss cheese configuration closer to the calculated bulk liquid conductivity from the french fry, we still see the affects of the nonuniformity of the system because the liquid is not in a symmetric slab with relatively flat edges as in the case of the french fry.

6.4.3 Extracting The Vapor Conductivity

A frequently-used technique for calculating the conductivity in liquid-vapor coexistence is to employ the lever rule, defined in Equation 6.4. This makes it possible to estimate the conductivity in coexistence based on the ratio of the two phases, as well as the values of the conductivity in the vapor phase and liquid phase on either side of the phase boundary curve. From the french fry configuration, we are able to extrapolate an estimate of the conductivity of the liquid phase, σ_{liq}. The Swiss cheese cell gives us the conductivity of the system in coexistence, σ_{coex}, for which we are using the trace of the conductivity tensor. We have implemented the lever rule using these two values, as well as the volume ratio of the liquid, to extract an estimate of the DC conductivity of the vapor phase, $\sigma_{vap} = 0.36 \pm 0.06$ x$10^5(\Omega m)^{-1}$.

$$\sigma_{coex} = \chi_{liq}\sigma_{liq} + (1 - \chi_{liq})\sigma_{vap} \tag{6.4}$$

6.5 Summary

For those simulations where we have compared the french fry and Swiss cheese configurations, we see a clear difference in the calculated electrical conductivity originating from the differences in the geometries of the systems. When dealing with a relatively symmetric geometry, such as the french fry, calculating an effective DC electrical conductivity is much more straightforward than in the case of an asymmetric structure. Because of the symmetry of the system, we were able to get an estimate of the DC electrical conductivity for the bulk liquid phase from the analysis of the french fry cell. We have found that the ionic geometry of a system plays a large role in determining the electrical conductivity.

6.6 Acknowledgements

Sandia National Laboratories is a multi-mission laboratory managed and operated by National Technology & Engineering Solutions of Sandia, LLC (NTESS), a wholly owned subsidiary of Honeywell International Inc., for the U.S. Department of Energy's National Nuclear Security Administration (DOE/NNSA) under contract DE-NA0003525. This written work is authored by an employee of NTESS. The employee, not NTESS, owns the right, title and interest in and to the written work and is responsible for its contents. Any subjective views or opinions that might be expressed in the written work do not necessarily represent the views of the U.S. Government. The publisher acknowledges that the U.S. Government retains a non-exclusive, paid-up, irrevocable, world-wide license to publish or reproduce the published form of this written work or allow others to do so, for U.S. Government purposes. The DOE will provide public access to results of federally sponsored research in accordance with the DOE Public Access Plan.

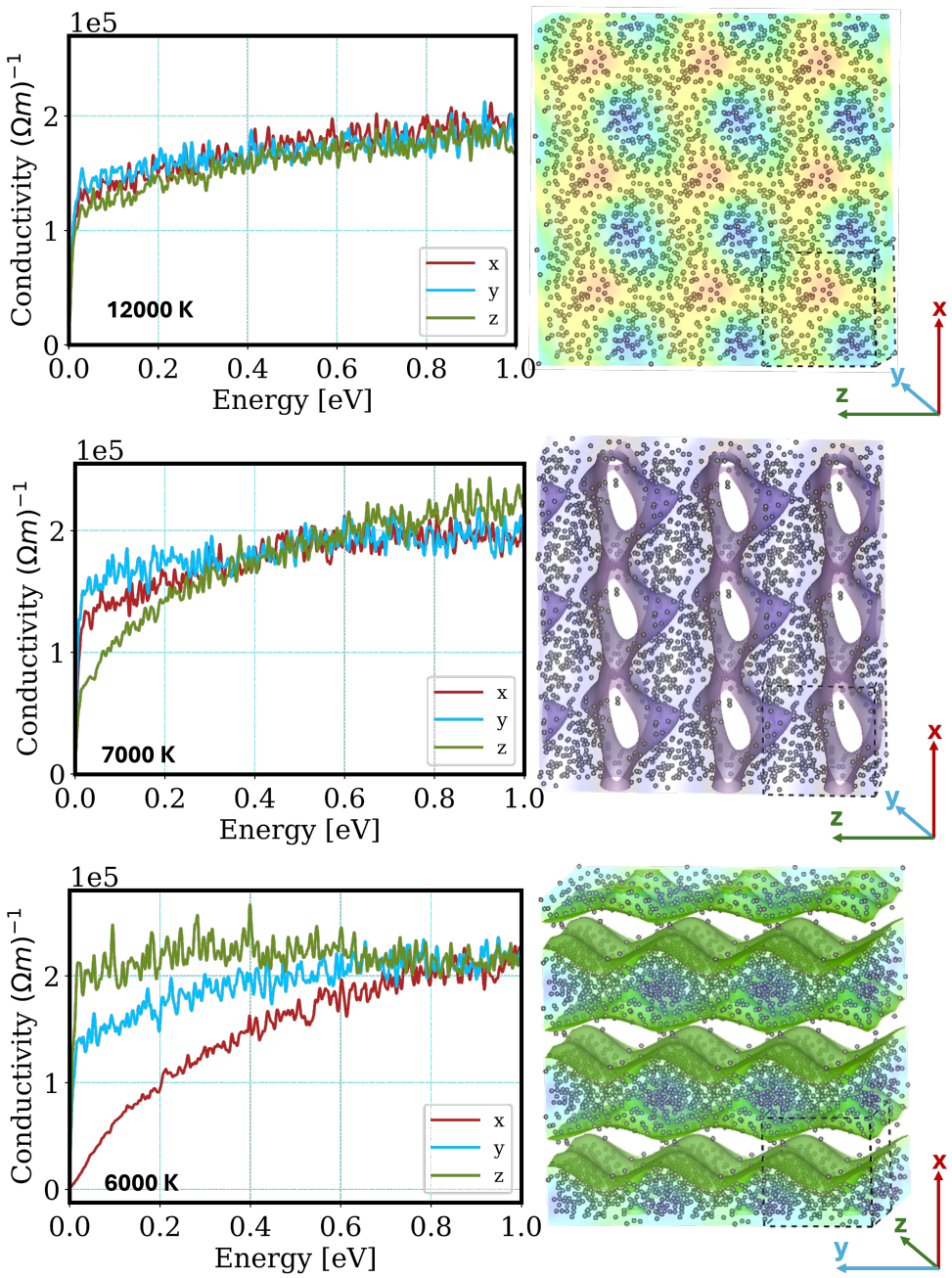

Figure 6.2: Component-separated Kubo-Greenwood electrical conductivity (left) for the Swiss cheese geometry at 12000 (top), 7000 (middle), and 6000 K (bottom), as well as the corresponding atomic configuration (right). The simulation cells has been replicated in space to enhance visualization.

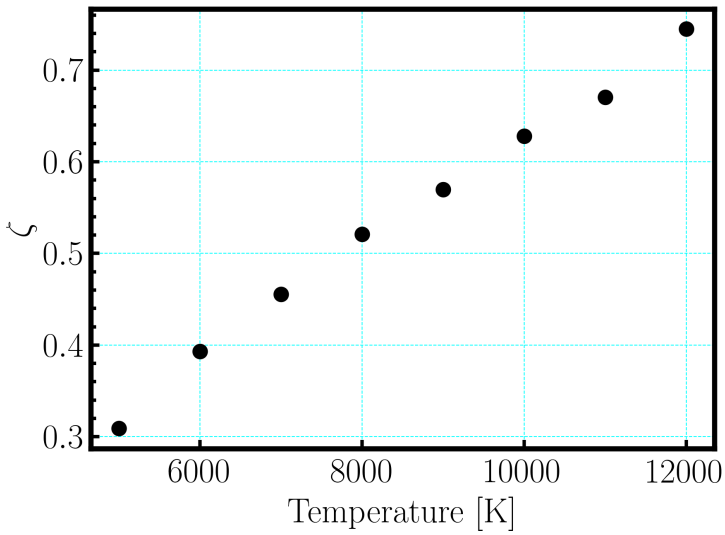

Figure 6.3: Calculated ζ values for a range of temperatures along the 5.00 g/cm^3 isochore. ζ is the normalized integral of the occupied density of states, shown in Equation 6.2, which approximately represents the average number of unbound electrons.

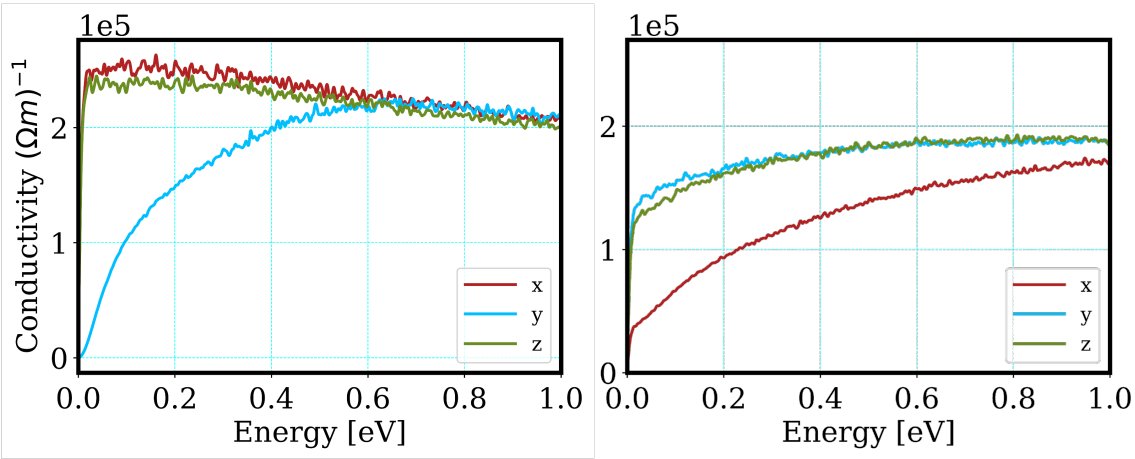

Figure 6.4: Time averaged *x, y,* and *z* components of the Kubo-Greenwood electrical conductivity at 5000 K and 5.00 g/cm^3. The plot on the left is for the french fry system, while the right image is for the Swiss cheese system.

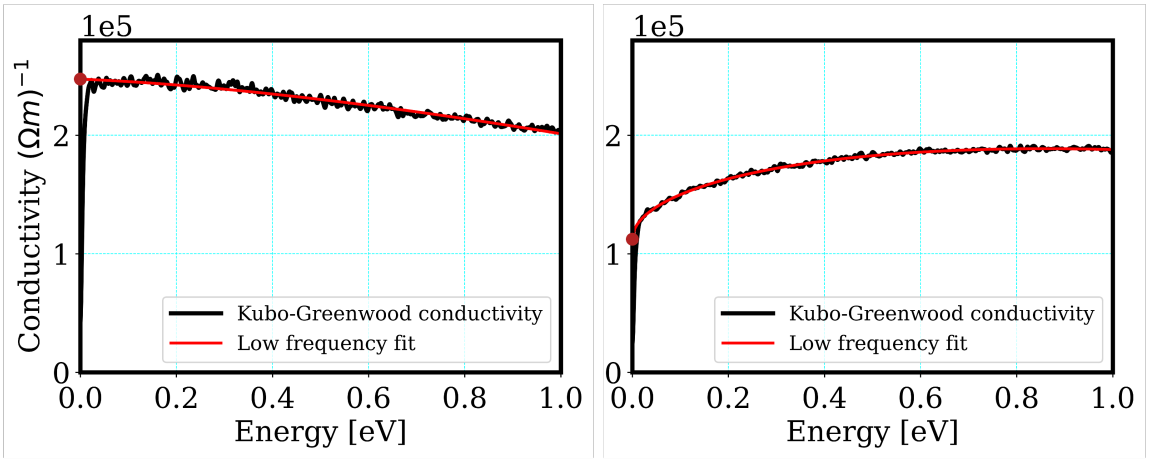

Figure 6.5: Average of the two largest components of the electrical conductivities shown in Figure 6.4 (black line) for the french fry (left) and Swiss cheese (right) configurations. The red line is a polynomial fit to the data at low frequencies. The fit has been extrapolated to zero frequency in order to calculate the DC electrical conductivity (red point).

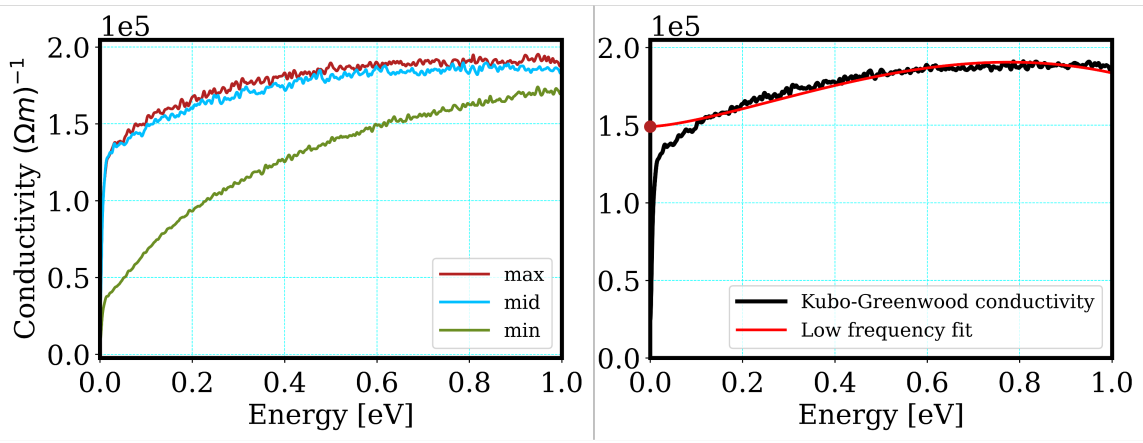

Figure 6.6: Average Swiss cheese conductivity for the maximum, minimum, and median values at each time step (left), as well as the extrapolation to the DC limit (right) excluding the minimum conductivity curve.

Chapter 7

Conclusions

The research in this dissertation has broadly focused on understanding material properties relevant to the high energy density physics experiments that are being done at the Sandia National Laboratories Z Pulsed Power facility. Sample materials in these experiments are regularly subjected to extreme conditions. To accurately interpret the data from these experiments, the materials involved, particularly the material standards, need to be fully characterized. In particular, there is a need for robust material equations of state. One example of a material standard that is used at Sandia is platinum. We have performed density functional theory molecular dynamics (DFTMD) simulations for a range of temperatures, densities, and number of atoms for platinum. The phase diagram of platinum near the liquid-vapor critical point and coexistence region has been characterized, finding a phase boundary curve that agrees very well with experimental data. The possible range of values of the critical point estimate has been narrowed. We have conducted an investigation of potential sources of bias in our calculations of the critical point and liquid-vapor phase boundary, finding that the size, geometry, method of separating the liquid and vapor

phases, as well as the well known approximations made within DFTMD all affect the critical point calculation. We have also begun an investigation of the transport properties of platinum within the liquid-vapor coexistence region.

References

[1] C. Desgranges, L. Widhalm, and J. Delhommelle, "Scaling laws and critical properties for fcc and hcp metals," *The Journal of Physical Chemistry B*, vol. 120, no. 23, pp. 5255–5261, 2016.

[2] V. E. Fortov, A. N. Dremin, and A. A. Leont'ev, "Evaluation of the parameters of the critical point," *Teplofizika vysokikh temperatur*, vol. 13, no. 5, pp. 1072–1080, 1975.

[3] G. R. Gathers, "Dynamic methods for investigating thermophysical properties of matter at very high temperatures and pressures," *Reports on Progress in Physics*, vol. 49, p. 341, apr 1986.

[4] A. L. Khomkin and A. S. Shumikhin, "The thermodynamics and transport properties of transition metals in critical point," *arXiv preprint arXiv:1606.09609*, 2016.

[5] M. M. Martynyuk, "Parameters of critical point of metals," *Zh. Fiz. Khim.*, vol. 57, pp. 810–821, 1983.

[6] D. A. Young and B. J. Alder, "Critical point of metals from the van der waals model," *Physical Review A*, vol. 3, no. 1, p. 364, 1971.

[7] N. B. Wilding, "Critical-point and coexistence-curve properties of the lennard-jones fluid: A finite-size scaling study," *Phys. Rev. E*, vol. 52, pp. 602–611, Jul 1995.

[8] T. M. Hartsfield and K. M. Amodeo, "Platinum liquid-vapor phase boundary mapped by fluid flyer experiments," *Phys. Rev. B*, vol. 111, p. 134115, Apr 2025.

[9] M. K. Lentz, J. P. Townsend, and M. P. Desjarlais, "Liquid-vapor coexistence of platinum from ab-initio simulations," *Submitted to J. Chem. Phys.*, 2025.

[10] M. Ohring, *Engineering materials science*. Academic Press, 1995.

[11] S. Dutta, K. Sankaran, K. Moors, G. Pourtois, S. V. Elshocht, J. Bommels, W. Vandervorst, Z. Tokei, and C. Adelmann, "Thickness dependence of the resistivity of platinum-group metal thin films," *Journal of Applied Physics*, vol. 122, p. 025107, 2017.

[12] E. Schrödinger, "An Undulatory Theory of the Mechanics of Atoms and Molecules," *Physical Review*, vol. 28, pp. 1049–1070, Dec. 1926.

[13] D. Griffiths and D. Schroeter, *Introduction to Quantum Mechanics*. Cambridge University Press, 2018.

[14] J. Jackson, *Classical Electrodynamics, 3rd Ed.* Wiley, 2007.

[15] F. Giustino, *Materials Modelling Using Density Functional Theory: Properties and Predictions*. Oxford University Press, 2014.

[16] N. Bohr, "I. On the constitution of atoms and molecules," *The London, Edinburgh, and Dublin Philosophical Magazine and Journal of Science*, vol. 26, no. 151, pp. 1–25, 1913.

[17] M. Born and R. Oppenheimer, "Zur quantentheorie der molekeln," *Annalen der Physik*, vol. 389, no. 20, pp. 457–484, 1927.

[18] J. C. Slater, "The theory of complex spectra," *Phys. Rev.*, vol. 34, pp. 1293–1322, Nov 1929.

[19] D. R. Hartree, "The wave mechanics of an atom with a non-Coulomb central field. Part I. theory and methods," *Mathematical Proceedings of the Cambridge Philosophical Society*, vol. 24, no. 1, p. 89–110, 1928.

[20] J. Nocedal and S. Wright, *Numerical Optimization*. Springer Series in Operations Research and Financial Engineering, Springer New York, 2006.

[21] V. Fock, "Näherungsmethode zur lösung des quantenmechanischen mehrkörperproblems," *Zeitschrift für Physik*, vol. 61, p. 126, 1930.

[22] P. Hohenberg and W. Kohn, "Inhomogeneous electron gas," *Phys. Rev.*, vol. 136, pp. B864–B871, Nov 1964.

[23] W. Kohn and L. J. Sham, "Self-consistent equations including exchange and correlation effects," *Phys. Rev.*, vol. 140, pp. A1133–A1138, Nov 1965.

[24] D. M. Ceperley and B. J. Alder, "Ground state of the electron gas by a stochastic method," *Phys. Rev. Lett.*, vol. 45, pp. 566–569, Aug 1980.

[25] C. Kittel, *Introduction to Solid State Physics*. Wiley series on the science and technology of materials, Wiley, 1976.

[26] A. Fetter and J. Walecka, *Quantum Theory of Many-particle Systems*. Dover Books on Physics, Dover Publications, 2003.

[27] J. P. Perdew and A. Zunger, "Self-interaction correction to density-functional approximations for many-electron systems," *Phys. Rev. B*, vol. 23, pp. 5048–5079, May 1981.

[28] N. Ashcroft and N. Mermin, *Solid State Physics*. HRW international editions, Holt, Rinehart and Winston, 1976.

[29] R. Martin, *Electronic Structure: Basic Theory and Practical Methods*. Cambridge University Press, 2020.

[30] G. Kresse and J. Hafner, "Ab initio molecular dynamics for liquid metals," *Phys. Rev. B*, vol. 47, pp. 558–561, Jan 1993.

[31] G. Kresse and J. Hafner, "Ab initio molecular-dynamics simulation of the liquid-metal–amorphous-semiconductor transition in germanium," *Phys. Rev. B*, vol. 49, pp. 14251–14269, May 1994.

[32] G. Kresse and J. Furthmüller, "Efficient iterative schemes for ab initio total-energy calculations using a plane-wave basis set," *Phys. Rev. B*, vol. 54, pp. 11169–11186, Oct 1996.

[33] G. Kresse and J. Furthmüller, "Efficiency of ab-initio total energy calculations for metals and semiconductors using a plane-wave basis set," *Computational Materials Science*, vol. 6, no. 1, pp. 15–50, 1996.

[34] M. L. Cohen, "Electronic structure of solids," *Physics Reports*, vol. 110, no. 5, pp. 293–309, 1984.

[35] J. P. Perdew and K. Burke, "Comparison shopping for a gradient-corrected density functional," *International Journal of Quantum Chemistry*, vol. 57, no. 3, pp. 309–319, 1996.

[36] J. P. Perdew, K. Burke, and M. Ernzerhof, "Generalized gradient approximation made simple," *Phys. Rev. Lett.*, vol. 77, pp. 3865–3868, Oct 1996.

[37] L. Haar, J. S. Gallagher, and G. S. Kell, *NBS/NRC steam tables thermodynamic and transport properties and computer programs for vapor and liquid states of water in SI units*. Hemisphere Publishing Corporation,New York, NY, 01 1984.

[38] Wikipedia contributors, "Cloud — Wikipedia, the free encyclopedia," 2025.

[39] G. L. Zabot, "Chapter 11 - Decaffeination using supercritical carbon dioxide," in *Green Sustainable Process for Chemical and Environmental Engineering and Science* (Inamuddin, A. M. Asiri, and A. M. Isloor, eds.), pp. 255–278, Elsevier, 2020.

[40] V. T. Minh, "Modeling and control of distillation column in a petroleum process," in *2010 5th IEEE Conference on Industrial Electronics and Applications*, pp. 259–263, 2010.

[41] R. Caracas and S. T. Stewart, "No magma ocean surface after giant impacts between rocky planets," *Earth and Planetary Science Letters*, vol. 608, p. 118014, 2023.

[42] F. Hensel and W. W. Warren, *Fluid Metals*. Princeton: Princeton University Press, 1999.

[43] E. U. Franck and F. Hensel, "Metallic conductance of supercritical mercury gas at high pressures," *Phys. Rev.*, vol. 147, pp. 109–110, Jul 1966.

[44] D. E. Fratanduono, M. Millot, D. G. Braun, S. J. Ali, A. Fernandez-Pa

nella, C. T. Seagle, J.-P. Davis, J. L. Brown, Y. Akahama, R. G. Kraus, M. C. Marshall, R. F. Smith, E. F. O'Bannon, J. M. McNaney, and J. H. Eggert, "Establishing gold and platinum standards to 1 terapascal using shockless compression," *Science*, vol. 372, no. 6546, pp. 1063–1068, 2021.

[45] S. Anzellini, V. Monteseguro, E. Bandiello, A. Dewaele, L. Burakovsky, and D. Errandonea, "In situ characterization of the high pressure- high temperature melting curve of platinum," *Scientific Reports*, vol. 9, 2019.

[46] N. C. Holmes, J. A. Moriarty, G. R. Gathers, and W. J. Nellis, "The equation of state of platinum to 660 GPa (6.6 Mbar)," *Journal of Applied Physics*, vol. 66, pp. 2962–2967, 10 1989.

[47] A. Porwitzky, J. Brown, S. Duwal, D. H. Dolan, C. Blada, J. Boerner, J. Williams, and S. Payne, "Reduced scale stripline platform to extend accessible pressures on the z machine: Shockless compression of platinum to 650 gpa," *Journal of Applied Physics*, vol. 132, p. 115102, 09 2022.

[48] K. R. Cochrane, P. Kalita, J. L. Brown, C. A. McCoy, J. W. Gluth, H. L. Hanshaw, E. Scoglietti, M. D. Knudson, S. P. Rudin, and S. D. Crockett, "Platinum equation of state to greater than two terapascals: Experimental data and analytical models," *Phys. Rev. B*, vol. 105, p. 224109, Jun 2022.

[49] V. M. Elkin, V. N. Mikhaylov, A. A. Ovechkin, and N. A. Smirnov, "A wide-range multiphase equation of state for platinum," *Journal of Physics: Condensed Matter*, vol. 32, p. 435403, jul 2020.

[50] P. R. Levashov, V. E. Fortov, K. V. Khishchenko, and I. V. Lomonosov, "Equation of state for liquid metals," *AIP Conference Proceedings*, vol. 505, pp. 89–92, 04 2000.

[51] G. Kresse and J. Hafner, "Ab initio simulation of the metal/nonmetal transition in expanded fluid mercury," *Phys. Rev. B*, vol. 55, pp. 7539–7548, Mar 1997.

[52] M. P. Desjarlais, "Quantum Molecular Dynamics Simulations for Generating Equation of State Data," in *Atomic Processes in Plasmas* (K. B. Fournier, ed.), vol. 1161 of *American Institute of Physics Conference Series*, pp. 32–38, AIP, Sept. 2009.

[53] B. Xiao and L. Stixrude, "Critical vaporization of mgsio_3," *Proceedings of the National Academy of Sciences*, vol. 115, no. 21, pp. 5371–5376, 2018.

[54] J. P. Townsend, G. Shohet, and K. R. Cochrane, "Liquid-vapor coexistence and critical point of mg 2 sio 4 from ab initio simulations," *Geophysical Research Letters*, vol. 47, no. 17, p. e2020GL089599, 2020.

[55] T. F. J. Bögels and R. Caracas, "Critical point and supercritical regime of mgo," *Phys. Rev. B*, vol. 105, p. 064105, Feb 2022.

[56] G. Kresse and D. Joubert, "From ultrasoft pseudopotentials to the projector augmented-wave method," *Phys. Rev. B*, vol. 59, pp. 1758–1775, Jan 1999.

[57] N. D. Mermin, "Thermal properties of the inhomogeneous electron gas," *Phys. Rev.*, vol. 137, pp. A1441–A1443, Mar 1965.

[58] M. K. Lentz, J. P. Townsend, and K. R. Cochrane, "DC electrical conductivity of platinum from ab initio simulations," *AIP Conference Proceedings*, vol. 2844, p. 320003, 09 2023.

[59] J. Clerk-Maxwell, "XXII. On the dynamical evidence of the molecular constitution of bodies," *J. Chem. Soc.*, vol. 28, pp. 493–508, 1875.

[60] F. J. Wegner, "Corrections to scaling laws," *Phys. Rev. B*, vol. 5, pp. 4529–4536, Jun 1972.

[61] R. K. Pathria and P. D. Beale, *Statistical Mechanics*. Amsterdam ; Boston: Elsevier/Academic Press, 3rd ed ed., 2011.

[62] O. K. R. Yamamoto and K. Nakanishi, "Can the 'van der Waals loop' vanish? ii. effect of domain size," *Molecular Physics*, vol. 84, no. 4, pp. 757–768, 1995.

[63] A. Z. Panagiotopoulos, "Direct determination of phase coexistence properties of fluids by monte carlo simulation in a new ensemble," *Molecular Physics*, vol. 100, pp. 237 – 246, 1987.

[64] M. Rovere, "Computer simulation of critical phenomena in fluids," *Journal of Physics: Condensed Matter*, vol. 5, p. B193, aug 1993.

[65] A. P. Willard and D. Chandler, "Instantaneous liquid interfaces," *The Journal of Physical Chemistry B*, vol. 114, no. 5, pp. 1954–1958, 2010. PMID: 20055377.

[66] J. Van Der Waals and J. Rowlinson, *On the Continuity of the Gaseous and Liquid States*. Dover Books on Physics Series, Dover Publications, 2004.

[67] H. Callen, *Thermodynamics*. New York: John Wiley and Sons, 1960.

[68] R. Yamamoto, H. Tanaka, K. Nakanishi, and X. Zeng, "Can the 'van der Waals loop' vanish?: Effect of surface free energy," *Chemical Physics Letters*, vol. 231, no. 4, pp. 401–406, 1994.

[69] K. Binder, B. J. Block, P. Virnau, and A. Tröster, "Beyond the Van Der Waals loop: What can be learned from simulating Lennard-Jones fluids inside the region of phase coexistence," *American Journal of Physics*, vol. 80, pp. 1099–1109, 12 2012.

[70] B. B. Karki, "First-Principles Molecular Dynamics Simulations of Silicate Melts: Structural and Dynamical Properties," *Reviews in Mineralogy and Geochemistry*, vol. 71, pp. 355–389, 01 2010.

[71] D. B. Sinars, M. A. Sweeney, C. S. Alexander, D. J. Ampleford, T. Ao, J. P. Apruzese, C. Aragon, D. J. Armstrong, K. N. Austin, T. J. Awe, A. D. Baczewski, J. E. Bailey, K. L. Baker, C. R. Ball, H. T. Barclay, S. Beatty, K. Beckwith, K. S. Bell, J. F. Benage, Jr., N. L. Bennett, K. Blaha, D. E. Bliss, J. J. Boerner, C. J. Bourdon, B. A. Branch, J. L. Brown, E. M. Campbell, R. B. Campbell, D. G. Chacon, G. A. Chandler, K. Chandler, P. J. Christenson, M. D. Christison, E. B. Christner, R. C. Clay, III, K. R. Cochrane, A. P. Colombo, B. M. Cook, C. A. Coverdale, M. E. Cuneo, J. S. Custer, A. Dasgupta, J. P. Davis, M. P. Desjarlais, D. H. Dolan, III, J. D. Douglass, G. S. Dunham, S. Duwal, A. D. Edens, M. J. Edwards, E. G. Evstatiev, B. G. Farfan, J. R. Fein, E. S. Field, J. A. Fisher, T. M. Flanagan, D. G. Flicker, M. D. Furnish, B. R. Galloway, P. D. Gard, T. A. Gardiner, M. Geissel, J. L. Giuliani, M. E. Glinsky, M. R. Gomez, T. Gomez, G. P. Grim, K. D. Hahn, T. A. Haill, N. D. Hamlin, J. H. Hammer, S. B. Hansen, H. L. Hanshaw, E. C. Harding, A. J. Harvey-Thompson, D. Headley, M. C. Herrmann, M. H. Hess, C. Highstrete, O. A. Hurricane, B. T. Hutsel, C. A. Jennings, O. M. Johns, D. Johnson, M. D. Johnston, B. M. Jones, M. C. Jones, P. A. Jones, P. E. Kalita, R. J. Kamm, J. W. Kellogg, M. L. Kiefer, M. W. Kimmel, P. F. Knapp, M. D. Knudson, A. Kreft, G. R. Laity, P. W. Lake, D. C. Lamppa, W. L. Langston, J. S. Lash, K. R. LeChien, J. J. Leckbee, R. J. Leeper, G. T. Leifeste, R. W. Lemke, W. Lewis, S. A. Lewis, G. P. Loisel, Q. M. Looker, A. J. Lopez, D. J. Lucero, S. A. MacLaren, R. J. Magyar, M. A. Mangan, M. R. Martin, T. R. Mattsson, M. K. Matzen, A. J. Maurer, M. G. Mazarakis, R. D. McBride, H. S. McLean, C. A. McCoy, G. R. McKee, J. L. McKenney, A. R. Miles, J. A. Mills, M. D. Mitchell, N. W. Moore, C. E. Myers, T. Nagayama, G. Natoni, A. C. Owen, S. Patel, K. J. Peterson, T. D. Pointon, J. L. Porter, A. J. Porwitzky, S. Radovich, K. S. Raman, P. K. Rambo, W. D. Reinhart, G. K. Robertson, G. A. Rochau, S. Root, D. V. Rose, D. C. Rovang, C. L. Ruiz, D. E. Ruiz, D. Sandoval, M. E. Savage, M. E. Sceiford, M. A. Schaeuble, P. F. Schmit, M. S. Schollmeier, J. Schwarz, C. T. Seagle, A. B. Sefkow, D. B. Seidel, G. A. Shipley, J. Shores, L. Shulenburger, S. C. Simpson, S. A. Slutz, I. C. Smith, C. S. Speas, P. E. Specht, M. J. Speir, D. C. Spencer, P. T. Springer, A. M. Steiner, B. S. Stoltzfus, W. A. Stygar, J. Ward Thornhill, J. A. Torres, J. P. Townsend, C. Tyler, R. A. Vesey, P. E. Wakeland, T. J. Webb, E. A. Weinbrecht, M. R. Weis, D. R. Welch, J. L. Wise, M. Wu, D. A. Yager-Elorriaga, A. Yu, and E. P. Yu, "Review of pulsed power-driven high energy density physics research on z at

sandia," *Physics of Plasmas*, vol. 27, 7 2020.

[72] M. Pozzo, M. P. Desjarlais, and D. Alfè, "Electrical and thermal conductivity of liquid sodium from first-principles calculations," *Phys. Rev. B*, vol. 84, p. 054203, Aug 2011.

[73] The POTCAR file used was PAW_PBE Pt_GW, 10Mar2009.

[74] L. Calderín, V. Karasiev, and S. Trickey, "Kubo–Greenwood electrical conductivity formulation and implementation for projector augmented wave datasets," *Computer Physics Communications*, vol. 221, pp. 118–142, 2017.

[75] M. P. Desjarlais, J. D. Kress, and L. A. Collins, "Electrical conductivity for warm, dense aluminum plasmas and liquids," *Phys. Rev. E*, vol. 66, p. 025401, Aug 2002.

[76] A. Kietzmann, B. Holst, R. Redmer, M. P. Desjarlais, and T. R. Mattsson, "Quantum molecular dynamics simulations for the nonmetal-to-metal transition in fluid helium," *Phys. Rev. Lett.*, vol. 98, p. 190602, May 2007.

[77] S. Mazevet, M. P. Desjarlais, L. A. Collins, J. D. Kress, and N. H. Magee, "Simulations of the optical properties of warm dense aluminum," *Phys. Rev. E*, vol. 71, p. 016409, Jan 2005.

[78] K. R. Cochrane, R. W. Lemke, Z. Riford, and J. H. Carpenter, "Magnetically launched flyer plate technique for probing electrical conductivity of compressed copper," *Journal of Applied Physics*, vol. 119, p. 105902, 03 2016.

[79] P. Grabowski, S. Hansen, M. Murillo, L. Stanton, F. Graziani, A. Zylstra, S. Baalrud, P. Arnault, A. Baczewski, L. Benedict, C. Blancard, O. Čertík, J. Clérouin, L. Collins, S. Copeland, A. Correa, J. Dai, J. Daligault, M. Desjarlais, M. Dharma-wardana, G. Faussurier, J. Haack, T. Haxhimali, A. Hayes-Sterbenz, Y. Hou, S. Hu, D. Jensen, G. Jungman, G. Kagan, D. Kang, J. Kress, Q. Ma, M. Marciante, E. Meyer, R. Rudd, D. Saumon, L. Shulenburger, R. Singleton, T. Sjostrom, L. Stanek, C. Starrett, C. Ticknor, S. Valaitis, J. Venzke, and A. White, "Review of the first charged-particle transport coefficient comparison workshop," *High Energy Density Physics*, vol. 37, p. 100905, 2020.

[80] L. J. Stanek, A. Kononov, S. B. Hansen, B. M. Haines, S. X. Hu, P. F. Knapp, M. S. Murillo, L. G. Stanton, H. D. Whitley, S. D. Baalrud, L. J. Babati, A. D. Baczewski, M. Bethkenhagen, A. Blanchet, I. Clay, Raymond C., K. R. Cochrane, L. A. Collins,

A. Dumi, G. Faussurier, M. French, Z. A. Johnson, V. V. Karasiev, S. Kumar, M. K. Lentz, C. A. Melton, K. A. Nichols, G. M. Petrov, V. Recoules, R. Redmer, G. Röpke, M. Schörner, N. R. Shaffer, V. Sharma, L. G. Silvestri, F. Soubiran, P. Suryanarayana, M. Tacu, J. P. Townsend, and A. J. White, "Review of the second charged-particle transport coefficient code comparison workshop," *Physics of Plasmas*, vol. 31, p. 052104, 05 2024.

[81] C. A. Melton, I. Clay, Raymond C., K. R. Cochrane, A. Dumi, T. A. Gardiner, M. K. Lentz, and J. P. Townsend, "Transport coefficients of warm dense matter from Kohn-Sham density functional theory," *Physics of Plasmas*, vol. 31, p. 043903, 04 2024.

[82] P. Tarazona, E. Chacón, and J. P. Hernandez, "Simple model for the phase coexistence and electrical conductivity of alkali fluids," *Phys. Rev. Lett.*, vol. 74, pp. 142–145, Jan 1995.

[83] R. Kubo, "Statistical-mechanical theory of irreversible processes. i. general theory and simple applications to magnetic and conduction problems," *Journal of the Physical Society of Japan*, vol. 12, no. 6, pp. 570–586, 1957.

[84] D. A. Greenwood, "The Boltzmann equation in the theory of electrical conduction in metals," *Proceedings of the Physical Society*, vol. 71, pp. 585–596, apr 1958.

[85] J. Dufty, J. Wrighton, K. Luo, and S. Trickey, "On the Kubo-Greenwood model for electron conductivity," *Contributions to Plasma Physics*, vol. 58, no. 2-3, pp. 150–154, 2018.